# INFORMATION TO USERS

This manuscript has been reproduced from the microfilm master. UMI films the text directly from the original or copy submitted. Thus, some thesis and dissertation copies are in typewriter face, while others may be from any type of computer printer.

**The quality of this reproduction is dependent upon the quality of the copy submitted.** Broken or indistinct print, colored or poor quality illustrations and photographs, print bleedthrough, substandard margins, and improper alignment can adversely affect reproduction.

In the unlikely event that the author did not send UMI a complete manuscript and there are missing pages, these will be noted. Also, if unauthorized copyright material had to be removed, a note will indicate the deletion.

Oversize materials (e.g., maps, drawings, charts) are reproduced by sectioning the original, beginning at the upper left-hand corner and continuing from left to right in equal sections with small overlaps.

ProQuest Information and Learning
300 North Zeeb Road, Ann Arbor, MI 48106-1346 USA
800-521-0600

**University of Alberta**

# Photoluminescence of Silicon Nanocrystal Superlattices

by

Megan Ann Glover 

A thesis submitted to the Faculty of Graduate Studies and Research in partial fulfillment of the requirements for the degree of Master of Science

Department of Physics

Edmonton, Alberta
Spring 2005

*In memory of my mother, Ann Glover,*
*who helped to instill in me a love of learning*

# Abstract

The mechanism of the photoluminescence of silicon nanocrystals has been hotly debated in recent years. Numerous models have been suggested to explain the strong luminescence, and many authors assume a particle size dependence of the emission spectrum (i.e., due to quantum confinement). Here, it will be shown that particle proximity effects can be more important than particle size in the luminescence of silicon nanocrystals. Several sets of specimens were synthesized in which the emission spectra were found to be highly sensitive to the microstructure of the specimens and nearly independent of particle size in size-selective excitation experiments. Using a multilayering approach where silicon nanoparticles were separated by "buffer" layers, the present work obtained strong evidence in favour of particle-to-particle carrier migration in silicon nanocrystal ensembles. The results show that size and, especially, interactions between nanoparticles must be independently controlled in order to isolate the different mechanisms responsible for the luminescence.

# Acknowledgements

Throughout my graduate work, I have been fortunate to have an excellent supervisor, Dr. Al Meldrum. I am grateful to Al for providing guidance throughout the project, including help with experiments, suggestions on writing, and many useful discussions.

Cindy Blois also deserves my thanks; she prepared the X-series specimens, assisted me with the microcavities preparation, and along with Al Meldrum, prepared specimens for TEM and took the images.

Thanks to Aaron Hryciw, who provided assistance on various experimental issues from time to time, and he designed a model that was used to determine active layer thicknesses for the microcavities. He also provided me with entertainment and camaraderie for two years whilst we shared an office

I am grateful to Greg Popowich, who taught me how to use the electron beam evaporation system, for his patience and guidance during that process. Thanks also to he and Don Mullin for providing great technical support during my use of the evaporation system.

Greg, Don, Aaron, and Cindy also deserve thanks for taking turns standing by to save me from possible electrocution while I was performing sample deposition.

Jesse McCrosky, in addition to calculating the interparticle spacing in my specimens, encouraged me always in my work, and believed more than I that I was capable of whatever task was put before me.

Finally, thanks to my family, for continually providing me with encouragement throughout my education.

# Table of Contents

**Chapter 1: Introduction** ..... **1**

1.1 Optical Properties of Silicon Nanocrystals ..... 1

1.2 Models of Silicon Nanocrystal Photoluminescence ..... 4

1.2.1 Overview ..... 4

1.2.2 Non-radiative Traps - The Effects of Surface Passivation ..... 4

1.2.3 Quantum Confinement Theory of Nanocrystal Photoluminescence 6

1.2.4 Photoluminescence From Surface States ..... 6

1.2.5 Reactive Nanocluster Model ..... 8

1.2.6 Erbium-doped Silicon Nanocrystals ..... 10

1.3 Photoluminescence Lifetimes ..... 10

1.4 Synthesis of Silicon Nanocrystals ..... 13

1.5 Silicon Nanocrystal Superlattices ..... 16

**Chapter 2: Experiment** ..... **20**

2.1 Sample Preparation ..... 20

2.2 Sample Characterization ..... 24

2.2.1 Transmission Electron Microscopy ..... 24

2.2.2 Transmission ..... 25

2.2.3 Photoluminescence Measurements ..... 25

2.2.4 Photoluminescence Dynamics Measurements ..... 27

**Chapter 3: Results** ..... **28**

3.1 Preliminary PL Results - Implications For Specimen Preparation ..... 28

3.2 Transmission Electron Microscopy ..... 30

3.3 Absorption and Photoluminescence ..... 36

3.3.1 X-series Results ..... 36

3.3.2 S-series Results ..... 37

3.3.3 O-series Results ..... 40

3.3.4 E-series Results ..... 42

**Chapter 4: Discussion** ..... **45**
4.1 Photoluminescence Spectral Shift: The Effect of Layer Thickness .. ..... 45
4.2 Effects of Layer Thickness On Emission Intensity ..... ..... 48
4.3 Effect of Particle Size ..... ..... 50
4.4 Excitation Lifetime in Silicon Nanocrystals: Effect of Layer Thickness ..... 53
4.5 Carrier Migration Across Buffer Layers..... ..... 57
4.5.1 $Er_2O_3$ Buffer Layers ..... ..... 57
4.5.2 $SiO_2$ Buffer Layers ..... ..... 61
4.6 Interactive Nanocluster Model ..... ..... 62
**Chapter 5: Wavelength Control** ..... ..... **67**
**Chapter 6: Conclusions** ..... ..... **73**
**References** ..... ..... **77**
**Appendix: Fitted Photoluminescence Spectra Results** ..... ..... **89**

# List of Tables

Table 2.1: List of specimens (number of layers, composition, layer thickness) 24

Table 3.1: Mean particle diameter values for specimens S1 through S4..... ..... 34

Table 5.1: Optical cavity specimens ..... ..... 74

Table A.1: Peak wavelength, integrated intensity, and FWHM of X-, S-, and O-series PL spectra ..... ..... 87

Table A.2: Peak wavelength, integrated intensity, and FWHM of S1 PL spectra excited at different wavelengths ..... ..... 88

Table A.3: Peak wavelength and integrated intensity of S-series specimens excited at different pump powers ..... ..... 88

# List of Figures

Figure 1.1: Absorption and PL spectrum of Si nanocrystals ..... 2
Figure 1.2: Estimated bandgaps for Si nanocrystals ..... 2
Figure 1.3: Bonding possibilities for silicon atoms on the surface of a nanocrystal 5
Figure 1.4: The reactive nanocluster model ..... 9
Figure 1.5: Energy levels of an erbium ion ..... 10
Figure 1.6: Schematic of energy transfer from a Si nanocrystal to an Er ion ..... 11
Figure 1.7: Comparison of a thick and a thin layer of silicon nanocrystals .. ..... 13
Figure 2.1: Schematic of electron beam evaporation set-up ..... 21
Figure 2.2: Photoluminescence experimental set-up ..... 27
Figure 3.1: PL spectra of specimen S1 with and without $SiO_2$ top layer ..... 28
Figure 3.2: PL spectra of specimen S1 after annealing in different gases ..... 30
Figure 3.3: PL spectra of a 250 nm SRO film annealed at different temperatures ... 31
Figure 3.4: Cross-sectional TEM images for specimens S2-S5 ..... 33
Figure 3.5: Electron diffraction image of nanoparticles, indexed to crystalline Si .. 34
Figure 3.6: Size distribution of Si nanoparticles in specimen S1 ..... 34
Figure 3.7: (a) Location of energy dispersive X-ray measurements on specimen S1;
(b) The specimen energy dispersive X-ray spectrum ..... 35
Figure 3.8: Transmission spectra of X-series specimens ..... 38
Figure 3.9: PL spectra of X-series specimens ..... 38
Figure 3.10: Transmission spectra of S-series specimens ..... 39
Figure 3.11: PL spectra of S-series specimens ..... 39
Figure 3.12: Excitation wavelength dependence of S1 PL spectra ..... 41
Figure 3.13: PL power dependence of specimen S4 ..... 41
Figure 3.14: PL time decay spectra, normalized to some initial intensity ..... 41
Figure 3.15: Transmission spectra of (a) O1-series and (b) O2-series ..... 43
Figure 3.16: PL spectra of O1-series ..... 43
Figure 3.17: PL spectra of O2-series ..... 44
Figure 3.18: Transmission spectra of specimens E-series ..... 45
Figure 3.19: PL spectra for E1 and E2 ..... 46

Figure 4.1: Gaussian curve fit to PL spectrum of specimen X4 ..... 48
Figure 4.2: PL peak wavelength dependence on SRO thickness for (a) the X-series specimens and (b) the S-series specimens ..... 49
Figure 4.3: Thickness-scaled PL spectra of (a) X-series; (b) S-series ..... 51
Figure 4.4: Capture area of non-radiative centres ..... 51
Figure 4.5: (a) Pump dependence of PL peak wavelength; (b) Pump wavelength dependence of S1 peak integrated intensity and peak wavelength ..... 53
Figure 4.6: Absorption versus integrated PL intensity at six excitation wavelengths 53
Figure 4.7: Fitted PL lifetime parameters ..... 55
Figure 4.8: Power dependence of (a) integrated intensity of PL peak and (b) PL peak wavelength of S-series specimens ..... 57
Figure 4.9: Power dependence of PL intensity at two different wavelengths ..... 58
Figure 4.10: Power dependence of nanocrystal PL intensity for specimen E2 . ..... 60
Figure 4.11: Power dependence of nanocrystal PL intensity and Er PL intensity ... 62
Figure 4.12: PL peak wavelength shift and integrated intensity change with $SiO_2$ thickness for the O-series specimens ..... 64
Figure 4.13: Relationship between peak PL wavelength and average transparency 68
Figure 5.1: Normalized PL spectra of nc-Si/$SiO_2$ superlattices ..... 70
Figure 5.2: Schematic of an optical cavity ..... 73
Figure 5.3: PL spectrum of a SRO specimen annealed at 500°C ..... 75
Figure 5.4: Normalized PL spectra of optical cavities ..... 75

# List of Symbols and Abbreviations

| | |
|---|---|
| $a_i$: | variables in background function used to analyse EDS spectra |
| $a_p$: | peak intensity of Gaussian function fit to PL spectrum |
| $\beta$: | dispersion factor (exponential "stretching") |
| CCD: | charged couple device |
| $C_O$: | atomic fraction of oxygen |
| $C_{Si}$: | atomic fraction of silicon |
| CW: | continuous wave |
| D: | deuterium |
| $d$: | active layer thickness [m] |
| $E$: | energy [J, eV] |
| e-beam: | electron beam vacuum evaporation |
| EDS: | Energy Dispersive X-ray Spectroscopy |
| E$i$: | where $i$ = 1, 2. Specimen series |
| $E_0^y$: | centroid of Gaussian function fit to EDS peaks, where $y$ = O, Si [eV] |
| FWHM: | full-width at half-maximum |
| HeCd: | Helium-Cadmium |
| InGaAs: | indium gallium arsenide |
| $I_O$: | integrated intensity of fitted oxygen EDS peak |
| $I_{Si}$: | integrated intensity of fitted silicon EDS peak |
| $I_y$: | intensity of Gaussian function fit to EDS peaks, where $y$ = O, Si |
| $k$: | wavenumber [$m^{-1}$] |
| $k_\alpha$: | primary characteristic X-ray |
| $k_{SiO}$: | correction factor in EDS analysis |
| $\theta$: | angle of incidence |
| $\lambda$: | wavelength [m] |
| $\lambda_p$: | peak wavelength of Gaussian function fit to PL spectrum [nm] |
| $N$: | EDS spectrum counts as a funtion of energy |
| n: | optical index of refraction |
| $N_B$: | EDS background function |

| | |
|---|---|
| $N_O$: | Gaussian function fit to the oxygen $k_\alpha$ peak |
| $N_{Si}$: | Gaussian function fit to the silicon $k_\alpha$ peak |
| nc-Si: | nanocrystalline silicon |
| O*iy*: | where $i$ = 1, 2 and $y$ = a, b, c, d. Specimen series |
| $P_b$: | Si dangling bond |
| PL: | photoluminescence |
| PSi: | porous silicon |
| $SiO_x$: | silicon-rich oxide, when $1 < x < 2$ |
| Si=O: | silicon-oxygen double bond |
| S*i*: | where $i$ = 1, 2, 3, 4, 5. Specimen series |
| SL: | superlattice |
| SRO: | silicon-rich oxide |
| $\sigma$: | width of Gaussian function fit to PL spectrum [nm] |
| $\sigma_y$: | width of Gaussian function fit to EDS peaks, where $y$ = O, Si [eV] |
| $\tau$: | photoluminescence lifetime [s] |
| TEM: | Transmission Electron Microscopy |
| UV: | ultraviolet |
| $\phi_i$: | phase change upon reflection from metal surface $i$ |
| X*i*: | where $i$ = 1, 2, 3, 4. Specimen series |
| $z$: | path length of wave [m] |

# Chapter 1: Introduction

Nanocrystalline silicon (nc-Si) has been widely studied ever since relatively intense photoluminescence (PL) was observed from porous silicon (PSi) and attributed to the effects of nanoscale silicon structures within the porous framework (Canham 1990). The widespread interest in porous silicon is due to the numerous potential applications associated with luminescent Si. However, PSi is mechanically fragile and susceptible to aging (Huy *et al.* 2003), to the degree that the development of photonic devices is problematic (Marsh 2002). In comparison, silicon nanocrystals embedded in an insulating host material are much more durable and may offer better potential for many types of silicon-based optical devices (*e.g.*, see Lockwood and Pavesi 2004, and references therein). Nanoscale silicon is currently one of the materials under investigation for applications such as LEDs, optical amplifiers, optical interconnects, and lasers (Klimov et al. 2000). Optical gain has been claimed in Si nanocrystals (Pavesi *et al.* 2000) although there has been debate over the validity of this report (Valenta *et al.* 2002; Elliman *et al.* 2003). The emission wavelengths can be tuned at least to some degree, by modifying the specimen microstructure (smaller particles, for example, are often claimed to emit at shorter wavelengths due to the quantum confinement effect; *e.g.*, Vinciguerra *et al.* 2000) or by the addition of impurities such as erbium (*e.g.*, Franzo *et al.* 1999) or carbon (Meldrum *et al.* 2004).

## 1.1 Optical Properties of Silicon Nanocrystals

Photoluminescence (PL) from nc-Si embedded in a matrix of $SiO_2$ typically peaks at wavelengths between 700-900 nm (see Figure 1.1). The emission has a quantum efficiency at least 4 orders of magnitude higher than that of bulk crystalline silicon (Canham

2000). Bulk silicon is a poor emitter because the excited electron-hole pairs have long lifetimes and are subject to a large capture cross section (Brus 1995). In nanocrystals, on the other hand, a non-radiative trap can, in theory, only quench the nanocrystal in which it resides. As well, the Auger effect is less prominent in Si nanocrystals because electron-hole pairs from separate nanocrystals should be more isolated from one another and therefore less free to interact. The work presented in this thesis will show that this simple picture is not strictly true in typical Si nanocomposites containing a high volume density of Si nanocrystals in an $SiO_2$ matrix.

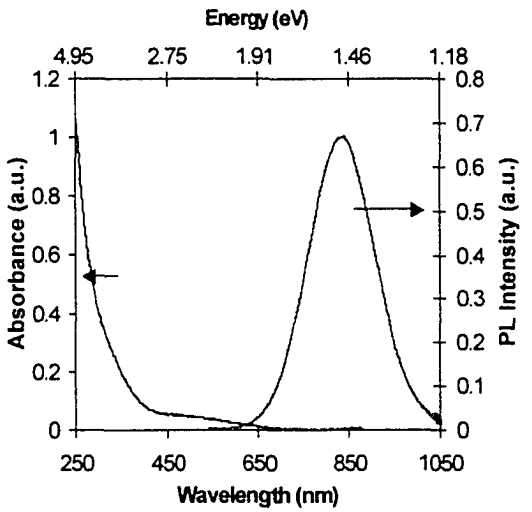


**Figure 1.1**: Absorption and PL spectrum from a "typical" specimen containing silicon nanocrystals embedded in $SiO_2$, showing the Stokes shift (difference between absorption onset and emission). Modified after Hryciw *et al.* (2004).

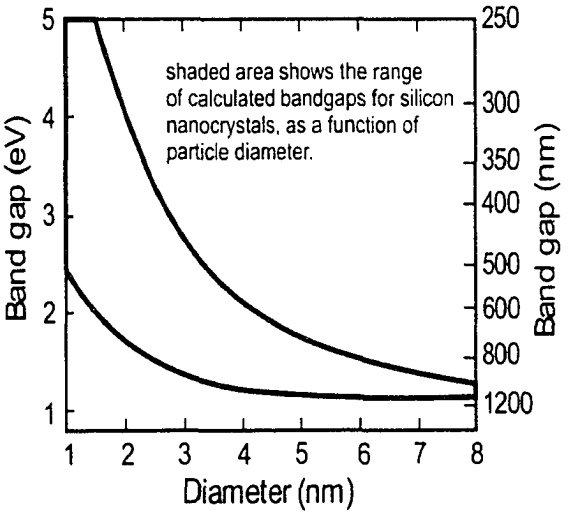


**Figure 1.2**: Variation in the theory results for the size dependence of the bandgap for Si nanocrystals, modified after Meldrum (2004). The bandgap is particle-size dependent, and becomes larger as the particles are made smaller. Note the large variation in the theoretical bandgap.

According to the effective mass approximation, the exciton Bohr radius of Si is approximately 5 nm. Particles with a radius smaller than this are in the "strong quantum confinement regime" and their minimum energy gap increases strongly as a function of decreasing particle size. Numerous theoretical approaches have been taken to calculate the

bandgap as a function of nanoparticle size (as well as the effects of surface passivation), with some considerable differences among the different models (see Figure 1.2). Nevertheless, the bandgap of nanoscale silicon is well above that of bulk Si and this is best reflected in the absorption spectra.

Silicon nanocrystals absorb strongly in the blue region of the visible spectrum but tend to be quite transparent in the red and near infrared (Figure 1.1). Thus silicon nanocrystals have a large characteristic Stokes shift (the difference between the absorption onset and the emission edge) of approximately 1.5 eV. Several authors have applied the Tauc method to obtain the optical gap from absorption data, and a range of values has been found; for example, White *et al.* found a value of 2.45 eV for a sample with an average particle diameter of 5 nm (1998) - slightly on the high side when compared to Figure 1.2. The absorption cross section for silicon nanocrystals depends strongly on nanocrystal size and excitation wavelength and ranges from $10^{-15} - 10^{-17}$ $cm^2$ depending on the particle size and absorption wavelength (Franzo, Vinciguerra, and Priolo 1999; Kenyon *et al.* 2002; Pavesi *et al.* 2000).

Some models have predicted that the bandgap of Si nanocrystals changes from indirect to a partially direct gap (Hill and Whaley 1995; Hybertsen 1994). No-phonon transitions may be "weakly allowed" due to the strong confinement of the electron and hole wavefunctions and the corresponding spreading in reciprocal space (Delerue *et al.* 2003). However, other calculations by Delerue *et al.* (2001) predict dominantly indirect-gap behavior for particle sizes as small as approximately 2 nm in diameter. Experiments also have been less than entirely conclusive on this point. For example, resonant PL spectroscopy investigations of the phonon structure in porous Si and Si nanocrystals suggested

a mostly direct-gap no-phonon behavior (Kovalev *et al.* 1998), but ultrafast transient absorption spectroscopy suggested an indirect gap in particles as small as 2.5 nm (Klimov *et al.* 1998). Hryciw *et al.* (2004) (as well as many others) observe lifetimes associated with the luminescence that are on the order of tens of microseconds - slower than direct gap II-VI compounds, for example, but considerably faster than bulk silicon. As suggested by Delerue et al. (2003), the optical gap nc-Si may have properties that reflect an "intermediate" band structure.

## 1.2 Models of Silicon Nanocrystal Photoluminescence

### 1.2.1 Overview

There are two major theories regarding the emission mechanisms of Si nanocrystals that I will discuss. One theory states that photoluminescence is due to the recombination of excitons across the quantum-confined bandgap (Section 1.2.3). The other theory says that absorption occurs across the confinement-enlarged bandgap but that the emission is due to a radiative center at the nanocrystal-matrix interface (Section 1.2.4). There are also various permutations and combinations of these fundamental theories.

In both theories, incident light of sufficient energy excites an electron across the gap, creating an electron-hole pair. These carriers typically have long radiative lifetimes in Si nanocrystals (as will be discussed in more detail later), although not as long as for crystalline silicon, where the lifetime is on the order of $10^{-4}$ - $10^{-3}$ s. At this point, both radiative and non-radiative recombination mechanisms can occur, and previous work on porous silicon has suggested that the photoluminescence lifetime is, in fact, controlled by non-radiative processes (Vial *et al.* 1992).

### 1.2.2 Non-radiative Traps - The Effects of Surface Passivation

One critical non-radiative trap in Si nanocrystals is Si dangling bonds (these go by the name of "$P_b$ centers" in the arcane nomenclature used in the "defect" literature), as shown in Figure 1.3. According to calculations by Delerue *et al.* (1993), one $P_b$ center on a nanocrystal has a large enough capture cross section to trap all excitons in that nanocrystal and thus prevent emission from (i.e, completely darken) the nanocrystal. The PL intensity has been shown to correlate inversely with the concentration of $P_b$ centers in a silicon nanocrystal composite, according to electron spin resonance measurements (Lopez *et al.* 2002).

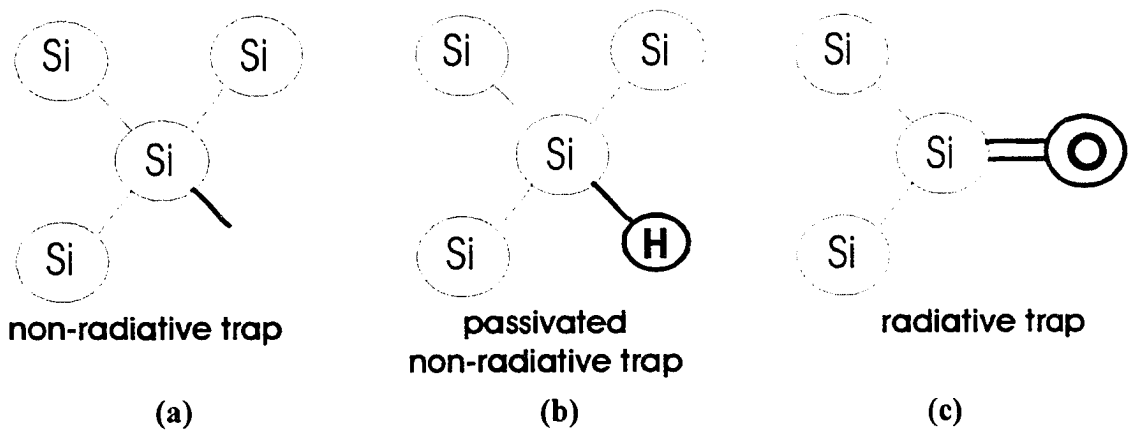


**Figure 1.3:** Bonding possibilities for silicon atoms on the surface of a nanocrystal. **(a)** a dangling Si bond acts as a non-radiative trap; **(b)** a hydrogen atom passivates the non-radiative trap; **(c)** a silicon-oxygen double bond acts as a radiative center, according to one theory of silicon nanocrystal photoluminescence.

A silicon $P_b$ center can be passivated by a hydrogen atom (see Figure 1.3), which is often achieved by annealing in a gas containing hydrogen. According to Min *et al.* (1996), implanting deuterium into samples of Si nanocrystals in $SiO_2$ increases the nanocrystal luminescence by a factor of ten, after the samples have been annealed at 500°C to allow for D migration and the recovery of radiation damage. The authors attributed the

increased luminescence to the mobility of the deuterium, and the subsequent bonding at $P_b$ centers on the $Si/SiO_2$ interface. Neufeld *et al.* (1997) observed that ion-implanted Si nanocrystals in $SiO_2$, when annealed in an atmosphere of $H_2/N_2$, show increased luminescence by a factor of three over vacuum-annealed samples. The PL increase was observed to be reversible, and was attributed to the hydrogen-passivation of non-radiative defects. Withrow *et al.* (1999) annealed Si nanocrystals embedded in $SiO_2$ in atmospheres containing either hydrogen or deuterium. From depth and concentration profiles of the H and D within the samples, they observed that upon the formation of Si nanocrystals at an annealing temperature of 1100°C, the H and D are no longer found in the bulk of the sample but only in the region where nanocrystals reside. The presence of hydrogen also dramatically increased the PL intensity while having almost no effect on the PL spectral distribution. The authors concluded that the results were consistent with a model of H passivating surface states at the $Si/SiO_2$ interface, leading to enhanced PL intensity.

### 1.2.3 Quantum Confinement Theory of Nanocrystal Photoluminescence

According to the quantum confinement theory of PL, the Si nanocrystals not only absorb across the quantum-confined bandgap, they also emit across it (with small Stokes shifts that can be due to a variety of processes such as exchange coupling and Coulomb interactions). Thus, in this model the observed light emission should be strongly particle size dependent (see Figure 1.2). Researchers have frequently observed that samples with smaller Si nanocrystals emit at shorter wavelengths, which they concluded to be consistent with emission across the bandgap (*e.g.*, Kenyon *et al.* 1998; Min *et al.* 1996). A PL blueshift with decreasing nanocrystal size is to be expected for emission across a bandgap that is changing with size, as illustrated in Figure 1.2. By etching away bigger or smaller parti-

cles, differently sized nanocrystals have been isolated in a single sample by Brongersma *et al.* (1999) and they also found a shift in the luminescence that was explained by recombination across the bandgap in differently-sized particles.

### 1.2.4 Photoluminescence From Surface States

The large Stoke's shift (~1-2 eV) observed in Si nanocrystals; however, is not consistent with a pure quantum confinement model. It seems clear (at least to this author) that there must be at least one other major process that occurs prior to photo-emission that *considerably* decreases the emission energy. Although there is still much debate in the literature, several workers have suggested that radiative centers (associated with oxygen) exist at the nanocrystal-matrix interface.

Theory has suggested that the bonding arrangement at this interface can produce radiative sub-gap (lower energy) states. Allan *et al.* (1996) performed calculations that showed that the Si bond at the Si-nanocrystal/oxide interface traps excitons when the silicon atom is bonded to a hydrogen atom, or bonded to another silicon atom in a $SiO_2$ molecule. According to this model, an Si-atom bonded to a hydrogen or another silicon atom creates a state at the nanocrystal-host interface that is slightly lower in energy than the optical absorption gap. However, in our specimens the Stokes shift is much larger than that predicted for Si-H or Si-Si interface bonds (see, for example, Delerue *et al.* 2003).

In an extension of the investigation of this role of surface states, Delerue *et al.* (1999) found that the Si=O double bond was a promising radiative center, as it formed a deep trap below the conduction band minimum. Wolkin *et al.* (1999) showed theoretically that in nanocrystals terminated only by hydrogen atoms (*i.e.*, no silicon-oxygen double bond), the recombination was from free exciton states (across the bandgap) for all nano-

particle sizes. However, for nanocrystals with one Si=O double bond, electrons can trap on the Si atom and holes can trap on the O atom. The recombination mechanism was proposed to be dependent on the nanocrystal size, since the radiative center can only be "stabilized" when the bandgap increases to a certain energy. According to the model, for a nanocrystal diameter greater than 2.9 nm, the recombination is via free excitons as the bandgap is not wide enough to stabilize the Si=O emission state; for a diameter less than 2.9 nm and greater than 1.6 nm the hole is free and the electron is trapped; and for a diameter less than 1.6 nm both the electron and hole are trapped. The predicted result is that oxidized samples exhibit a decrease in the emission energy when compared to hydrogen-passivated non-oxidized samples, especially for the smallest nanocrystals.

Interestingly, the Si=O radiative center has been purely theoretical, and there is, to my knowledge, only one example where there is any direct experimental evidence for it (the large Stokes shift is *consistent* with the theoretical picture of Si=O surface bonds, but this evidence is indirect at best). Polar phonon scattering and photoluminescence measurements (Garrido *et al.* 2000) showed that the Stokes shift is almost exactly twice the energy of a Si=O vibration mode that is 0.134 eV. The authors contend the dominant emission is therefore assisted by the local Si=O vibration, spatially located at the Si-$SiO_2$ interface. These observations supported the idea of a silicon-oxygen interface-related radiative sub-gap state.

There are also indications that trapped carriers may not be as localized if there is more than one oxygen atom bonded to a nanocrystal's surface (this is very likely the common case for nanocrystals embedded in a matrix of $SiO_2$). Vasiliev *et al.* (2000) found, theoretically, that with more oxygen on the surface of a nanocrystal, the calculated optical

gap decreases as a result of interactions among oxygen-induced electronic states. The oxygen atoms create trapped electron and hole states that reduce the effective size of the bandgap. The PL redshift often observed for larger Si nanocrystals may be then due to more surface silicon atoms available for bonding in larger nanocrystals, rather than owing to the smaller bandgap of larger nanoparticles.

### 1.2.5 Reactive Nanocluster Model

A "reactive nanocluster" model (see Figure 1.4) of Si nanocrystal luminescence involving surface trapping of excitons and nanocrystal proximity effects has been recently developed by Iwayama *et al.* (1998; 1999; 2001). In that model, excitons are created by a photon absorption across the bandgap, but then are rapidly trapped by a Si=O radiative center. The sub-10 ps relaxation of photo-induced absorption associated with the quantized states that has been observed (Klimov *et al.* 1998) is consistent with the model's proposed fast-trapping scheme. The nanocrystals are only separated by a thin oxide (exactly how thin is not specified in the model) and a decrease in the energy levels of the states at the nanocrystal-

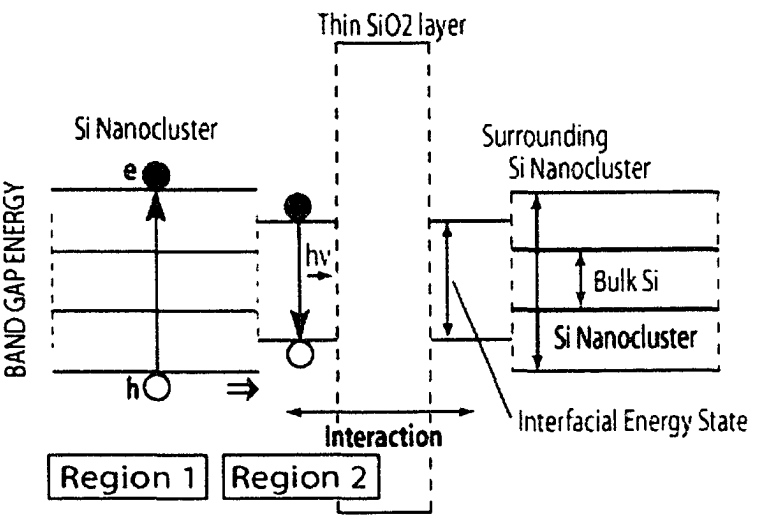


**Figure 1.4:** The reactive nanocluster model, after Iwayama *et al.* (1998; 2001). An electron is excited across the quantum confinement widened bandgap (Region 1). It relaxes to a state at the nanocrystal-oxide interface where it can emit radiatively (Region 2). The interfacial energy states can interact through the thin oxide layer, resulting in a lowering of the energy level. After Iwayama *et al.* (1998).

oxide interface results. For nanocrystals that are more closely spaced, a photoluminescence redshift would then be observed. According to Iwayama *et al.* (1998), this so-called "reactive nanocluster model" could explain why samples with larger nanoparticles are often observed to have red-shifted PL: in effect, these samples have higher concentrations of silicon which results in bigger particles that are also *more closely spaced.* However, the authors are vague on the nature of the interaction mechanism. In fact, the energy-lowering mechanism is not discussed in the three similar papers published by these authors, from which Figure 1.4 was extracted.

### 1.2.6 Erbium-doped Silicon Nanocrystals

Much of the interest in silicon nanocrystal photonics is associated with the strong 1.5 micron emission observed in Er-doped silicon nanocrystal composites. An energy-level diagram of the erbium ion $Er^{3+}$ is shown in Figure 1.5. The transition from the $^4I_{13/2}$ excited state to the $^4I_{15/2}$ (ground) state corresponds to the principle transparency window in optical fibers at ~1540 nm. For this reason, silica glass lightly doped with Er ions is commonly used in optical fiber amplifiers. Unfortunately, these amplifiers need a very specific pump

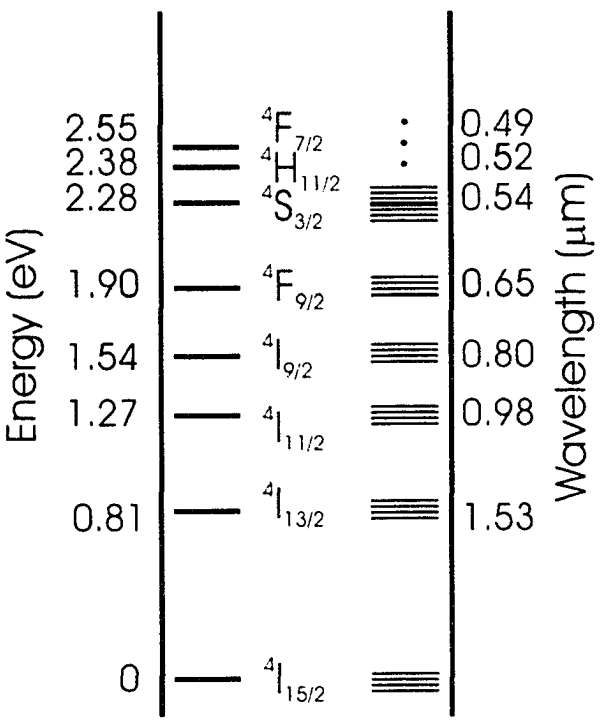


**Figure 1.5:** Energy levels of an erbium ion ($Er^{3+}$). The transition from $^4I_{13/2}$ to $^4I_{15/2}$ corresponds to the principal transparency window in optical fibers. Modified after Polman (1997).

wavelength (corresponding to the transition from the ground state to a higher erbium level, *e.g.*, the $^4I_{11/2}$ level, or the higher Stark-split sublevels of the $^4I_{13/2}$ band) and they also have relatively low gain so that the amplifying section of fiber must be long.

Erbium doping of silicon nanocrystals allows the nanocrystal radiative center to transfer energy non-resonantly via phonons (see Figure 1.6), probably to the two lowest excited states of $Er^{3+}$ (Priolo *et al.* 2001b). Thus, the nanocrystals act as *sensitizers* for the $Er^{3+}$ luminescence. The excited electron can subsequently relax to the ground state through infrared light emission. This nonresonant excitation of erbium opens the door to less expensive broadband pumping that does not have to specifically match any of the erbium energy levels.

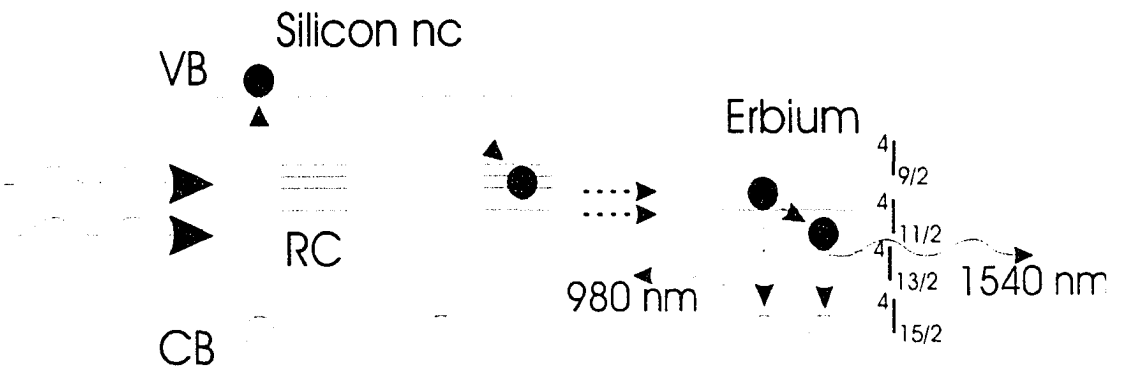


**Figure 1.6:** Schematic of energy transfer from a Si nanocrystal to an Er ion. An incident photon excites an electron from the conduction band (CB) to the valence band (VB) in a silicon nanocrystal (nc). The electron transfers non-radiatively to the nanocrystal radiative center (RC), but instead of de-exciting radiatively, it transfers its energy to an excited state of an erbium ion. The erbium ion subsequently emits in the infrared. Modified after Priolo *et al.* (2001b).

It was not clear for some time where the Er ions are in relation to the Si nanocrystals, but most evidence now points to the Er ions being in the $SiO_2$ matrix *outside* the nanoparticles (*e.g.*, Fujii *et al.* 1998; Franzo *et al.* 1999). The transfer mechanism has not been conclusively identified, although a phonon mediated Auger effect may be one candidate mechanism. The concentration of Er ions is important to the intensity of the 1540 nm

emission - too little Er will result in a weak PL, but too much Er can also reduce the PL intensity due to concentration quenching effects (Polman 1997). Er-doped silicon nanocrystal composites are now widely investigated for potential application in waveguide amplifiers, and the nanocrystal-to-erbium energy transfer will be employed in the present work to experimentally prove the operation of effective nanocrystal-to-nanocrystal charge migration processes.

## 1.3 Photoluminescence Lifetimes

A range of lifetimes has been observed for silicon nanocrystal luminescence, with lifetime values being on the order of tens to hundreds of microseconds, depending on the emission wavelength (*e.g.*, Linnros *et al.* 1999), the particle size and proximity (*e.g.*, Priolo et al. 2001b), and specimen structure (*e.g.*, single films versus multi-layer films: Iacona *et al.* 2001b). Most authors explain that shorter wavelengths have shorter PL lifetimes because the low-wavelength emission is due to smaller nanoparticles, which have faster dynamics as predicted by quantum confinement models. This effect is specifically attributed to greater "electron-hole wavefunction overlap" in small particles (Vala *et al.* 2001); however, it ignores the complicating effects of radiative centers and interactions on the emission wavelength (*i.e.*, it is a strict quantum-confinement-based explanation). One could even speculate that the effect is not directly a result of quantum confinement at all; but is due to a manifestation of Fermi's golden rule, which describes the increase in optical mode density with frequency for spontaneous radiation.

In most reports, the PL decay is found to follow a stretched exponential function given by:

$$I = I_0 e^{-\left(\frac{t}{\tau}\right)^{\beta}} \qquad (1.1)$$

where $I_0$ is the initial intensity, $t$ is time, $\tau$ is the decay lifetime, and $\beta$ is a dispersion factor that indicates the deviation of the function from an single exponential form (sometimes referred to as the "stretching" of the exponential). The dispersion factor can have values between zero and one, with a dispersion factor equal to one giving a single exponential form. The stretching is thought to be due to disorder: random exciton tunneling among nanocrystals of different sizes (Pavesi and Cheschini 1993; Pavesi 1996), or random carrier escape to non-radiative recombination sites (Vial *et al.* 1992; Mihalescu *et al.* 1996). If these models are correct, than $\beta$ corresponds to disorder, and smaller values of $\beta$ should be observed in samples where particles are separated by smaller distances, in which interparticle effects might be stronger.

Some researchers have observed that $\beta$ approaches unity when the specimen consists of multiple layers of nanocrystals as compared to single thicker films. This has been attributed to the decreasing effect of random carrier migration and recombination in thinner layers in which there are fewer interacting neighbours (Iacona *et al.* 2001b; Priolo *et al.*

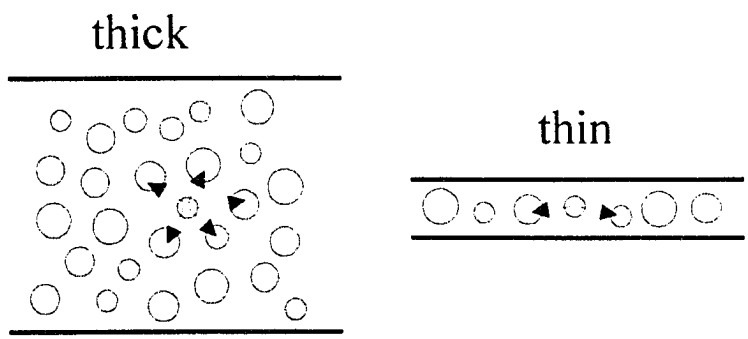


**Figure 1.7:** A comparison of a thick and a thin layer of silicon nanocrystals (cross sectional view). Nanocrystals in a thin layer have fewer neighbouring nanocrystals to interact with.

2001a), although presumably migration could still occur *within* a layer of nanoparticles. Single exponential decays ($\beta = 1$) have been reported in multilayered samples (Iacona *et al.* 2001b;). This was attributed to spatial isolation of the nanoparticles, minimizing interactions (*i.e.*, "disorder") that leads to stretched exponential decays. Further complicating the picture, it has also been shown theoretically that a stretched exponential decay can be produced for a *single* nanocrystal with single trap and single recombination center, and that disorder may not be required (Chen 2003). If this is the case, it would conflict with observations that isolated nanocrystals approximate single exponential luminescence decay (*e.g.*, Vinciguerra *et al.* 2000).

## 1.4 Synthesis of Silicon Nanocrystals

Common techniques used to make Si nanocrystal samples are chemical vapor deposition, vacuum evaporation (e-beam), physical sputtering, ion implantation, pulsed laser deposition, and chemical precipitation. In this work, electron beam evaporation is used because it offers control over the layer thickness, the ability to easily fabricate multiple separate layers, and the ability to "reactively" evaporate source materials in the presence of $O_2$, allowing for the synthesis of $SiO_x$ with $x > 1$.

To form Si nanoclusters, the specimen must subsequently be exposed to high temperatures in order to induce phase separation of Si and $SiO_2$. For $x$ values between 1 and 2, the thermodynamically (although not kinetically) favored phase assemblage is $Si+SiO_2$, hence the requirement for high-temperature thermal processing. The optimal temperature and annealing environments have been investigated for ion implanted samples in particular (Neufeld *et al.* 1997; Cheylan and Elliman 1999; Withrow *et al.* 1999; Lopez *et al.*

2002), but for thin films there is not as much systematic work on the thermal processing conditions. For ion implanted samples the most intense luminescence is achieved when annealing at temperatures between 1000°C and 1200°C in $Ar+H_2$, because at these temperatures the hydrogen diffuses into the sample and passivates non-radiative centers (Withrow *et al.* 1999). Despite these findings, samples produced by thin film methods have generally been processed in an $N_2$ atmosphere.

For thin films, one generally wants to avoid annealing at too high a temperature (especially for Si-rich films) or one may obtain very large nanocrystals or even possibly a semi-continuous layer of silicon. Some researchers have reported larger particles forming at higher anneal temperatures in ion implanted samples (Sharma *et al.* 1999). Others report that larger particles form after longer anneal times, although these conclusions were not made directly using techniques like transmission electron microscopy, but indirectly by examining absorption spectra and PL redshifts (Soni *et al.* 1999). Lopez *et al.* (2001) found that annealing for 1 minute versus 16 hours did not change the nanocrystal size but the PL intensity did saturate after 4 hours due to complete H passivation.

The electron beam evaporation method for producing Si nanocrystal films was pioneered by Kahler and Hofmeister (2001), and it is particularly important for this thesis. They found that the size of silicon nanocrystals (measured by high resolution TEM) made by electron beam evaporation could be controlled by the oxygen pressure in the bell jar during evaporation. They varied the oxygen pressure between $1.5 \times 10^{-7}$ Torr and $7.5 \times 10^{-5}$ Torr, and, after annealing all specimens at 1000°C in an argon atmosphere, they found a strong dependence of the luminescence spectrum on the oxygen pressure. The PL intensity increased for nanocrystals prepared in oxygen pressures from

$1.5 \times 10^{-7}$ Torr up to $3.8 \times 10^{-6}$ Torr and the PL peak blueshifted slightly. Increasing the pressure further (up to $7.5 \times 10^{-5}$ Torr) resulted ultimately in a decreased PL intensity, while the PL peak continued to blueshift. The strongest PL, from the specimen prepared in $3.8 \times 10^{-6}$ Torr oxygen pressure, is an order of magnitude stronger than the PL from the weakest-emitting specimen (prepared in $7.5 \times 10^{-5}$ Torr of oxygen). TEM results showed that the mean nanocrystal size decreased with increasing oxygen pressure, and the overall film composition became more oxygen rich. The maximum PL intensity occurred when the nanocrystals were $3.7 \pm 0.35$ nm in size and the chemical composition was $SiO_{1.5}$. The peak wavelength of the nanocrystal emission decreased continuously as the particle size decreased, but the authors did not investigate this trend in any detail.

To dope nc-Si specimens with erbium, $Er^{3+}$ ions can be implanted into the host material in the case of ion implanted specimens. In thin film techniques, erbium can be deposited (*e.g.*, from an $Er_2O_3$ or metallic Er source) simultaneously with the deposition of silicon and oxygen. In this thesis, I hoped to employ the efficient transfer of energy from silicon nanocrystals to erbium ions in order to shed light on nanocrystal interaction effects (*i.e.*, I was not specifically studying the Er emission but instead using the erbium to investigate interactions between silicon nanoparticles, as discussed below). Hence, for this work, $Er_2O_3$ layers were deposited in films separate from the nanocrystal-containing layers.

## 1.5 Silicon Nanocrystal Superlattices

Most recently, some researchers have focused on layers of silicon nanocrystals separated by "buffer" layers of $SiO_2$ to form superlattice structures (*e.g.*, Vinciguerra *et al.* 2000; Iacona *et al.* 2001b; Zacharias *et al.* 2002; Yi *et al.* 2002). In all of these previous studies of multilayer structures, the deposition of ultra-thin layers of elemental silicon was used to produce the nanocrystals; this thesis is among the first work to use $SiO_x$ as the "active" (*i.e.*, emitting) part of a multilayer superlattice.

Increased luminescence efficiency in thinner active layers has been observed in nc-Si/$SiO_2$ SL specimens prepared by plasma-enhanced chemical vapor deposition (Vinciguerra *et al.* 2000). The Si layers consisted of single planes of Si nanocrystals, the size of which varied from 1.1-2.3 nm as a function of increasing silicon layer thickness. The weaker PL intensity for thicker layers was attributed to the presence of particles too large to exhibit quantum-confinement-enhanced luminescence.

Enlargement of the bandgap with decreasing nanoparticle size was used to explain the blueshift observed by Vinciguerra *et al.* (2000) for thinner nc-Si layers separated by at least 5 nm of $SiO_2$. Iacona *et al.* (2001b) compared the above nc-Si/$SiO_2$ SL specimens to single-layer $SiO_x$ films (about 200 nm thick) with the same nanoparticle sizes, as measured by TEM. The $SiO_x$ films have redshifted PL spectra compared to their corresponding superlattice PL spectra. Iacona *et al.* concluded that because the nanocrystals in the $SiO_x$ films are, on average, closer together than in the multilayered films, more energy transfer from smaller (higher energy bandgap) to larger (lower energy bandgap) nanocrystals can occur. This results in a lowering of the emission energy (a PL redshift). The mechanism for energy transfer was not discussed.

A change in PL spectra with nanoparticle size was observed by Zacharias *et al.* (2002). Superlattices consisting of layers of nc-Si less than 3.8 nm thick separated by 2-3 nm layers of $SiO_2$ were prepared by reactive evaporation of SiO powder in an $O_2$ atmosphere. A blueshift in the PL spectra was observed for some specimens with smaller nanoparticles, which the authors described as being consistent with pure quantum confinement theory, but no systematic trend with decreasing particle size was reported.

A PL blueshift in nc-Si/$SiO_2$ SL specimens also occurs when the excitation power is increased (Vinciguerra *et al.* 2000). This phenomenon is also observed in single thick films of nanocrystals. For example, Hryciw *et al.* (2004) observed a blueshift from 827 to 811 nm when the pump power was increased from 5 to 16 mW, all other factors being kept constant. This shift has been attributed to the saturation of the slower dynamics in the red part of the emission spectrum. Some authors (*e.g.*, Vinciguerra *et al.* 2000) attribute this directly to the effects of particle size (faster dynamics in smaller particles).

As discussed in Section 1.3, the PL decay in multilayers consisting of one-nanocrystal-thick "active" layers separated by thicker "inactive" $SiO_2$ layers has been fit with single exponentials, giving unusually long lifetimes of ~300 $\mu$s. The presence of a single exponential decay instead of the typical stretched exponential decay was attributed to the nanoparticles being well isolated due to their in-plane separation of ~3 nm. In another study (Iacona *et al.* 2001b) in which the nanocrystal spacing was controlled by making films with different compositions (varying the Si concentration), the film with the most isolated nanoparticles exhibited a high $\beta$ value and a long lifetime, while the films with a higher concentration of nanoparticles were characterized by lower $\beta$ values and shorter

lifetimes (Iacona *et al.* 2001b). The authors stated that low β values- indicated "extensive energy transfer" amongst the closely-spaced particles.

Yi et al. (2002) examined the dependence of PL on the thermal processing temperature for superlattices prepared by reactive evaporation of SiO powders in an $O_2$ atmosphere. The absorption and PL were compared to that of a "bulk" SiO film (presumably, a very thick film of SiO - the thickness was not specified) and a "bulk" $SiO_2$ film prepared under same the conditions. Three PL bands were observed in the samples annealed at varying temperatures: a band at 560 nm that disappeared at temperatures above 700°C, a second band at 760-890 nm that begins above 500°C and then "transforms" into a third band centered in the infrared above 900°C. These three bands were associated with three stages of phase separation. Between 100°C and 600°C a transformation from silicon atoms possibly bonded in either ring- or chain-like structure into Si rings alone was reported. These ring-like arrangements were proposed to form a kind of proto-nanocluster at temperatures from 600°C to 900°C. TEM images showed that the SiO layers are amorphous for annealing temperatures up to 900°C. The amorphous clusters crystallize above 900°C into the Si nanocrystals, as studied previously by Zacharias *et al.* (2002).

The previous work has suggested that particle interactions may be important in the PL of silicon nanocrystals; however, it has proven difficult to isolate the effects of nanocrystal *size* from those of nanocrystal *separation*. In this thesis, I will present the first systematic studies in which particle size is clearly not a factor - all my samples are produced in the same way and have particles of the *same* size, within the limits of our technique. In this way, I will investigate experimentally what we now call the "interactive nanocluster" model, in which energy can flow from particle to particle and thereby control the lumines-

cence spectrum. It can be observed that this model differs from the "reactive nanocluster" model proposed by Iwayama *et al.* (1998; 1999; 2001), which does not invoke carrier migration. To do this, I will examine systematically the effects of nanocrystal spacing by using inactive buffer layers of $SiO_2$ in order to separate individual layers of nanoparticles in a controlled way. I will show, for the first time, that the emission wavelength *can be tuned over a range of more than 160 nm without changing the nanocrystal size or composition of the film.* This effect, which I attribute to nanocrystal interactions, may be potentially useful in photonic devices that require specific wavelengths to be produced from silicon nanoparticles. This work will show conclusively that for silicon nanocrystals embedded in silicon oxide, particle size effects in the luminescence are almost insignificant in comparison to the effects of particle spacing.

# Chapter 2: Experiment

The experimental focus of this thesis is on a series of silicon nanocrystal superlattices, in which buffer layers separate the nanocrystalline (active) layers. The buffer layers are composed of either silicon dioxide or erbium oxide. Silicon dioxide was chosen as the buffer layer material for most specimens because it does not absorb at the wavelengths used for excitation and is electrically insulating. Thus, it can act as a separating layer without interfering with the PL of the nc-Si. The $Er^{3+}$ levels in $Er_2O_3$ only luminesce when excited resonantly, but in principle the erbium ions can also be excited by an energy transfer from Si nanocrystals. With erbium oxide acting as a buffer layer, the migration of charge carriers through the nanocrystal layers to the buffer layers can be investigated by observing the luminescence due to erbium.

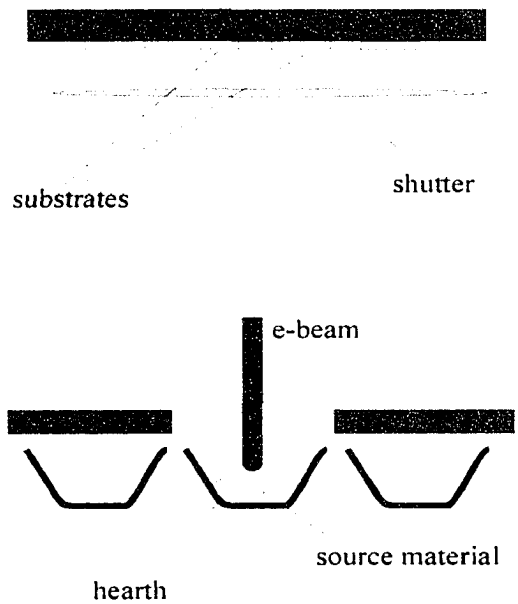


**Figure 2.1:** Schematic of electron beam evaporation set-up. The source material in the exposed hearth is evaporated when the e-beam strikes it. The evaporated material is deposited on the substrate above.

## 2.1 Sample Preparation

All samples were prepared by electron beam evaporation of the appropriate source materials. Specimens were prepared on optical quality (Esco Products Type A1) fused quartz wafers cleaned in methanol. The substrates were held directly over the hearth in which the source materials were placed (see Figure 2.1). The system has many hearths, and can be rotated so that only one hearth is exposed at any given time. The electron beam

can only evaporate the source material in the hearth that is open. To aid this work, we devised a way to load numerous substrates and shutter them individually, or all at once.

When I first began preparing specimens, I was the only one using the new electron beam gun and multi-hearth system that our group had recently for the thin film laboratory, and I found that specimens produced at different times were encouragingly reproducible. The S-series and E-series specimens were prepared in this one-by-one manner. However, as other research groups began to use the electron beam system to evaporate different materials with different setups than my own, I found that it became increasingly difficult to reproduce identical conditions between samples prepared at different times. This is quite important, because the nc-Si films were found to be sensitive to oxygen flow and the positioning of various components in the evaporation system. Therefore, for specimens produced later in this thesis work (the X-series, O1-series, and O2-series), our shuttering system permitted several different specimens to be grown *simultaneously*, under identical processing conditions. Since in the following work we wanted to eliminate particle size effects, comparisons (in terms of PL intensity, PL peak wavelength, etc.) can be made *within* a series, but not *between* them since the different series were prepared at different times.

The source materials were nominally 99.99% pure SiO (to produce the Si-nanocrystal-containing layers), 99.999% pure $SiO_2$, and 99.99% $Er_2O_3$. Source materials were placed in molybdenum crucibles for evaporation, and the crucible containing SiO had a tungsten lid (with a small hole in it) which prevented excessive gettering (absorption of gases) during evaporation. All materials were evaporated in a low pressure of flowing oxygen. The oxygen pressure in the bell jar was set to a constant pressure of $1 \times 10^{-5}$ Torr

before the evaporation, which resulted in pressures during the evaporation of $(4 \pm 1) \times 10^{-6}$ Torr for SiO, $(7 \pm 1) \times 10^{-6}$ Torr for $SiO_2$, and $(1 \pm 1) \times 10^{-5}$ Torr for $Er_2O_3$. The pressure differences are due to oxygen gettering during evaporation.

The thickness of individual layers was monitored using a crystal thickness monitor, into which source-material-specific information (density, acoustic impedance) were input from tables. The specimens were shuttered when the reading on the thickness monitor reached the desired layer thickness. From trials with different specimens, it seems that the thickness monitor tends to underestimate the true thickness by ~30%, due to the uncalibrated tooling factor. Therefore, for my specimens it was necessary to perform TEM measurements on a few specimens to obtain true values for the thicknesses. Then, assuming the tooling factor doesn't change for the other specimens, the thickness of new specimens can be estimated.

All aspects of the sample preparation were held as constant as was possible so as not to cause the resulting nanoparticles to differ in size from one sample to another within each series. Special care was taken with the oxygen pressure, due to the sensitivity noted by Kahler and Hofmeister (2001), as well as in my own observations. Specimens produced early-on in the project (the S-series and the E-series, as described below) were prepared individually but under identical conditions, as I was the sole user of our new electron beam system at the time. Specimen series produced later in the project (X-series and O-series, as described below) were prepared simultaneously using our shuttering system, to ensure preparation under identical conditions within the same series.

Four series of samples were prepared, and their specifications are given in Table 2.1. The X-series consists of four single-layer specimens of silicon-rich oxide (SRO),

**Table 2.1:** List of specimens. The active layers are silicon nanocrystals, produced by evaporation of silicon monoxide in a partial pressure of oxygen to produce a silicon-rich oxide (SRO). The topmost layer (on the surface) is always the buffer layer.

| Sample | Active Layer | | Buffer Layer | | |
|---|---|---|---|---|---|
| | thickness (nm) | number | thickness (nm) | number | composition |
| X1 | 200 | 1 | 20 | 1 | $SiO_2$ |
| X2 | 100 | 1 | 20 | 1 | $SiO_2$ |
| X3 | 50 | 1 | 20 | 1 | $SiO_2$ |
| X4 | 13 | 1 | 20 | 1 | $SiO_2$ |
| S1 | 200 | 1 | 100 | 1 | $SiO_2$ |
| S2 | 75 | 4 | 20 | 4 | $SiO_2$ |
| S3 | 20 | 9 | 20 | 10 | $SiO_2$ |
| S4 | 10 | 20 | 20 | 20 | $SiO_2$ |
| S5 | 4 | 10 | 20 | 10 | $SiO_2$ |
| O1a | 20* | 4 | 0 | 0 | $SiO_2$ |
| O1b | 20 | 4 | 5 | 4 | $SiO_2$ |
| O1c | 20 | 4 | 10 | 4 | $SiO_2$ |
| O1d | 20 | 4 | 15 | 4 | $SiO_2$ |
| O2a | 20* | 4 | 0 | 0 | $SiO_2$ |
| O2b | 20 | 4 | 2 | 4 | $SiO_2$ |
| O2c | 20 | 4 | 4 | 4 | $SiO_2$ |
| O2d | 20 | 4 | 6 | 4 | $SiO_2$ |
| E1 | 20 | 10 | 20 | 10 | $Er_2O_3$ |
| E2 | 20 | 10 | 1 | 10 | $Er_2O_3$ |

* Effectively 80 nm of continuous SRO

varying in thickness from 13 nm to 200 nm. The S-series of samples consisted of SRO layers ranging in thickness from 4 nm to 200 nm, separated by $SiO_2$ buffer layers 20 nm thick. For the O1- and O2-series (prepared at different times), $SiO_2$ layers of varying thickness were used to separate 20 nm layers of SRO. In series O1, the $SiO_2$ layers were 0, 5, 10, or 15 nm thick in specimens O1a, O1b, O1c, and O1d, respectively. Series O2 was identical, except that the buffer layers were 0, 2, 4, and 6 nm thick. In the E-series, the SRO layers were also 20 nm thick but were separated by 1 nm or 20 nm of $Er_2O_3$. All X-, S-, and O-series specimens were capped with a buffer layer of $SiO_2$ to limit possible oxidation or hydration of the SRO layer closest to the surface. The E-series specimens had a layer of $Er_2O_3$ on the top surface.

To produce silicon nanocrystals within the SRO layers, all samples except the O2-series were annealed for 1 hour at 1000°C in flowing gas maintained slightly above atmospheric pressure. The annealing gas was Ar + $H_2$ (4% or 10%), selected after an extensive trial of various annealing ambients (see Section 3.1). The O2 series of specimens was annealed in $N_2$ + $H_2$(5%). The annealing temperature was also chosen for providing the strongest PL. Further evidence supporting these choices of annealing environments will be provided in the Chapter 3.

## 2.2 Sample Characterization

### 2.2.1 Transmission Electron Microscopy

Cross-sectional specimens were prepared for transmission electron microscopy by standard thinning and ion milling procedures. Specimens were analyzed on the JEOL 2010 $LaB_6$ instrument in the Department of Physics. Although this instrument is not suit-

able for high-resolution imaging due to the large-gap polepieces currently installed, standard bright-field imaging was used to investigate the basic specimen microstructure. Electron diffraction was used to identify the crystal structure of the nanoparticles observed in the images, and energy dispersive X-ray analysis, using the fused quartz specimen substrate as a standard, was performed on one specimen to determine the chemical composition of the active layer.

### 2.2.2 Transmission

The transmission spectra were obtained by measuring the light transmitted through each specimen from a broadband lamp, and collected using a fiber optic CCD system. The percent transmission at wavelength $\lambda$ is given by:

$$T_\lambda = \frac{S_\lambda - D_\lambda}{R_\lambda - D_\lambda} \times 100 \qquad (2.1)$$

and the absorbance at $\lambda$ is given by:

$$A_\lambda = -log_{10}\left(\frac{S_\lambda - D_\lambda}{R_\lambda - D_\lambda}\right) \qquad (2.2)$$

where $S_\lambda$ is the light intensity (transmitted through the specimen from the blackbody source) at $\lambda$ received by the spectrometer, $R_\lambda$ is the light intensity at $\lambda$ when the specimen is not present, and $D_\lambda$ is the "dark" response at $\lambda$ when the light source is shuttered.

The absorbance in terms of the transmission is then:

$$A_\lambda = -log_{10}\left(\frac{T_\lambda}{100}\right) \qquad (2.3)$$

The transmission spectrum of a blank fused quartz wafer, identical to those used as specimen substrates, showed that the substrate does not absorb at wavelengths longer than

250 nm (see Figure 3.8). The wavelengths used to excite the PL were all above 300 nm, so the substrate did not interfere with the excitation or photoluminescence processes.

### 2.2.3 Photoluminescence Measurements

For all specimens except those in the E-series, the 325 nm line of a HeCd laser was used as the excitation source. The beam had a diameter of ~1 $mm^2$ and a CW power of ~20 mW. The photoluminescence spectra were collected using a fiber-coupled 2048-pixel linear array CCD spectrometer normalized to a blackbody reference source. This normalization procedure corrects for the spectral response of the CCD/grating combination. Care was taken not to disturb the setup between sample measurements, as it was found that even small changes in fiber position can change the amount of light collected and alter the relative intensity measurements.

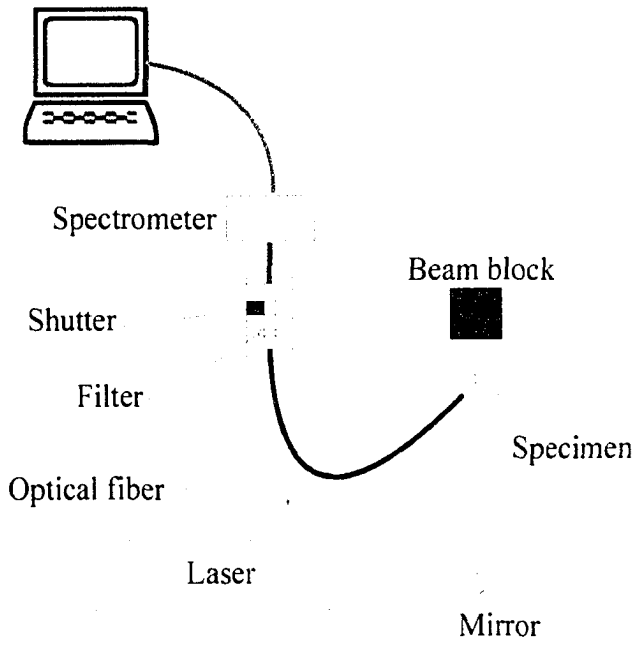


**Figure 2.2:** Photoluminescence experimental set-up. Laser light is brought, with the aid of a mirror, on to the specimen. An optical fiber collects the light emitted from the specimen. A filter is used to eliminate the intense laser light before it is collected by a CCD spectrometer. The data is collected and analyzed on a computer.

To collect PL spectra for the E-series samples for both resonant excitation (using the 488 nm line of an Ar laser, which is resonant with the $^4I_{15/2}$ to $^4F_{7/2}$ transition in $Er^{3+}$) and non-resonant excitation (using the 476.5 nm Ar line which is not matched to any $Er^{3+}$ transition), the same basic setup was used, except the powers ranged from 20 to 2300 mW.

A 512 pixel linear InGaAs array spectrometer was used to collect the spectra above 900 nm in wavelength. The Ar laser was also used to excite the S-series samples in order to investigate the power dependence of the PL spectra.

To examine the pump wavelength dependence of the photoluminescence spectra, the 325 nm and 442 nm lines of the HeCd laser and the 456 nm, 476 nm, 488 nm and 514 nm lines of the Ar laser were used. Every effort was made to keep excitation conditions as similar as possible at the different wavelengths, using a pump power of 20 mW and a laser spot size of close to 1 $mm^2$.

### 2.2.4 Photoluminescence Dynamics Measurements

PL lifetime measurements were done using a pulsed laser (operated at 4 kHz) that emits ~10 ns pulses at a wavelength of 349 nm with an average power of 30 mW. The luminescence was passed through a long-pass filter to remove any reflected or scattered laser light and was collected on a silicon photodiode that was interfaced to an 8-bit 200 MHz digital oscilloscope. To reduce noise fluctuations in the final spectra, the oscilloscope was set to average 128 individual measurements. These were the first experiments we did using this lifetime system and, through this work, we found several ways to optimize the system in the future. Later experiments will use a 32-bit multichannel analyzer and a more sensitive detector in order to improve the resolution of the measurements.

# Chapter 3: Results

## 3.1 Preliminary PL Results - Implications For Specimen Preparation

All specimens in the X-, S-, and O-series were made with a top layer 20 nm thick, in order to protect the uppermost SRO layer from possible oxidation or hydration. This was done on the advice of K-H Heinig (Rossendorf) who has unpublished data suggesting that exposure to atmosphere can affect the PL of nc-Si. Although the diffusion rate is unknown, a 20-nm-thick cap of $SiO_2$ was judged to be sufficient to prevent atmospheric contamination (we have observed that silver films can be protected from oxidizing for several months, using an identical capping layer). Additionally, the presence of the capping layer appeared to slightly affect the PL intensity (Figure 3.1). In order to ensure consistency, therefore, a 20-nm-thick $SiO_2$ cap was used as the top layer on all other X-, S-, and O- series specimens. However, it seems that some ageing still occurs, despite the 100-nm-thick top layer, as PL spectra of both samples taken 6 months after the original spectra (Figure 3.1) show both spectra converging to similar intensities. Whether the PL intensity of the sample without $SiO_2$ is decreasing, or the PL intensity of the $SiO_2$-topped sample is increasing, or both, is unclear as there is no absolute standard to measure against. It seems

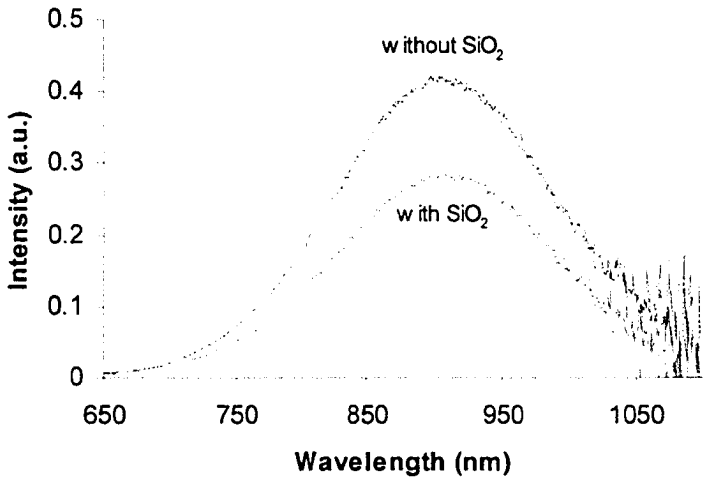


**Figure 3.1**: PL spectra of specimen S1 (200 nm nc-Si and 100 nm $SiO_2$) and specimen S1 without the $SiO_2$ capping layer (nc-Si is exposed to atmosphere).

likely that prolonged exposure to atmosphere is causing the change in PL brightness, and it would be interesting to systematically investigate the effects of ageing samples in different gases. For the PL measurements below, all data was taken at the same time in order to "average out" any possible aging effects within the different series. Indeed, subsequent analysis of the data sets showed the same trends as for the measurements taken at earlier times.

In addition to investigating the effects of the capping layer, preliminary experiments were done to determine the optimum annealing temperature and atmosphere. PL spectra were measured for four equivalent pieces of specimen S1 that were each annealed at 1000 °C in Ar + $H_2$, $N_2$ + $H_2$, Ar, or $N_2$. As can be seen from these spectra in Figure 3.2, the most intense luminescence was produced for the specimen annealed in Ar + $H_2$, followed by the specimen annealed in $N_2$ + $H_2$. In general, the presence of hydrogen results in an increased PL intensity, and Ar was found to be slightly better than nitrogen in this respect. For this reason Ar + $H_2$ was used to anneal all specimens except the O2 series. Specimens annealed in Ar + 10%$H_2$ were compared with specimens annealed in Ar + 4%$H_2$, and no consistent differences in the PL spectra of the resulting nanocrystals were observed.

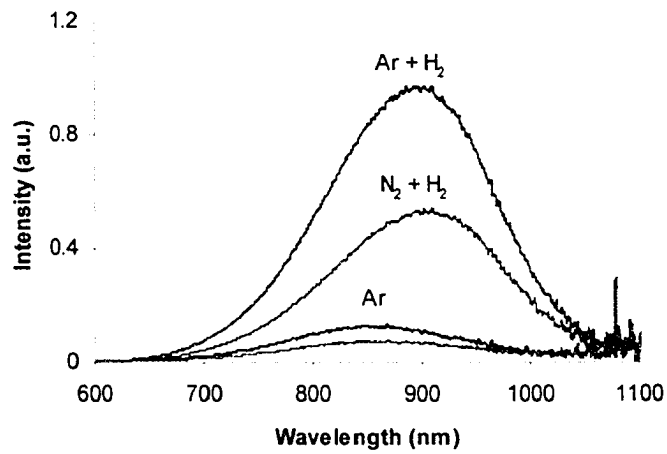


**Figure 3.2**: PL spectra of specimen S1 after annealing at 1000°C for 1 hour in different gases. The spectra after an anneal in $N_2$ is not labelled for clarity, but lies directly under the Ar spectrum.

An annealing temperature of 1000°C was used because it was found to produce the most intense luminescence as compared to films annealed at 600°C, 800°C, 1000°C, and 1200°C (Figure 3.3). Annealing at only 600°C produces a low intensity, broad luminescence peaked at ~700 nm. Other work (Yi *et al.* 2002) suggests that nanocrystals do not form at such low temperatures, and that instead structures such as Si rings and amorphous clusters are responsible for this type of luminescence. After processing at 800°C, the PL is slightly lower in intensity and shifted to lower energies as compared to the 600°C anneal. The specimen annealed at 1000°C is only slightly redshifted from the 800°C specimen, but it is an order of magnitude more intense. After annealing at 1200°C, no luminescence can be detected. The specimen appeared completely clear to the eye and exhibited excellent transmission in the range of 200 to 900 nm. It is possible that the film cracked or broke off the surface, as serious cracking or film delamination problems are not unusual at such high temperatures. Based on this set of preliminary experiments, all specimens investigated were annealed at 1000°C in Ar + $H_2$ except for the O2-series specimens, which were annealed at 1000°C in $N_2$ + $H_2$.

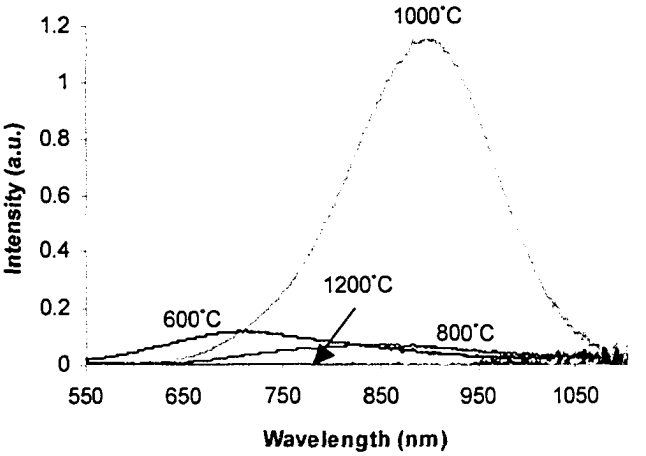


**Figure 3.3:** PL spectra of a 250-nm-thick SRO film annealed for 1 hour in Ar + (10%)$H_2$ at different temperatures. No detectable PL was observed for the specimen annealed at 1200°C.

## 3.2 Transmission Electron Microscopy

The cross-sectional TEM images for the S-series are shown in Figure 3.4. These images were used to verify the actual thicknesses of the layers in the S-series samples (as given in Table 2.1), to estimate the average size and size distribution of the nanoparticles, and to confirm the identification of the nanoparticles as crystalline silicon. Since specimen preparation is a laborious and time-consuming process, the TEM measurements focused on this set of samples only. The electron-diffraction patterns conclusively identified the nanoparticles as crystalline silicon, and the nanoparticles are randomly oriented (see Figure 3.5). From these images, the average particle diameters and standard deviations were found for specimens S1 through S4. These data are listed in Table 3.1, and a representative histogram for specimen S1 is shown in Figure 3.6. Images of specimen S5 showed that the active layers, which were 4 nm thick, were actually Si nanocrystals distributed in single planes; however, there were too few clearly observable nanocrystals to obtain statistically significant particle counts. The particle counting and measuring was done manually using digital imaging software, counting over 200 particles for each specimen. Due to the typically low contrast difference between Si nanoparticles and the $SiO_2$ matrix, there is naturally some error in judging the edges of the particles in these measurements.

**Figure 3.4**: Cross-sectional TEM images for specimens S2-S5. The silicon nanocrystals are imaged as dark spots, while the $SiO_2$ layers have a lighter contrast. Arrows point to specimen surfaces.

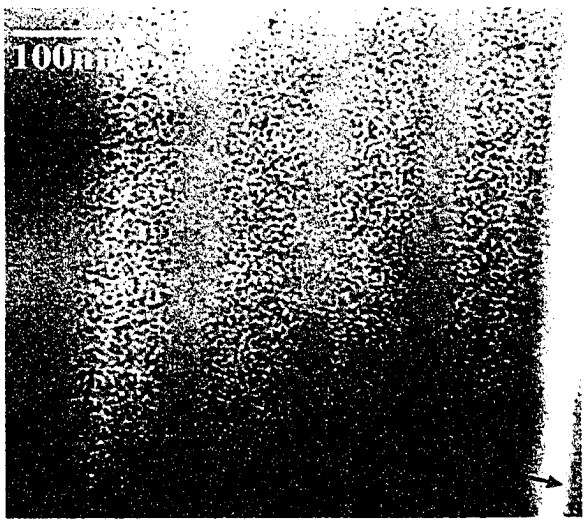


**(a)** Specimen S2, having four nc-Si layers each 75 nm thick.

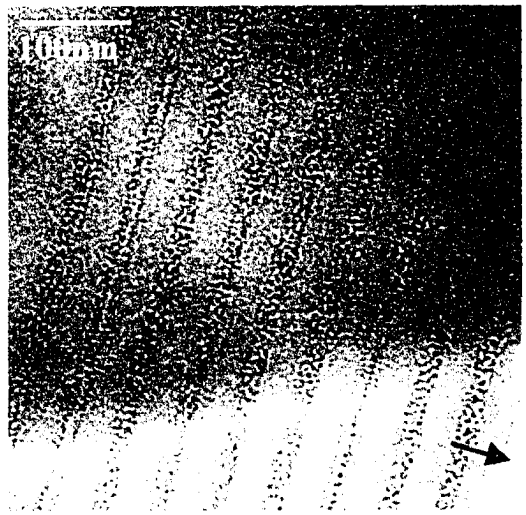

**(b)** Specimen S3, having nine nc-Si layers each 20 nm thick.

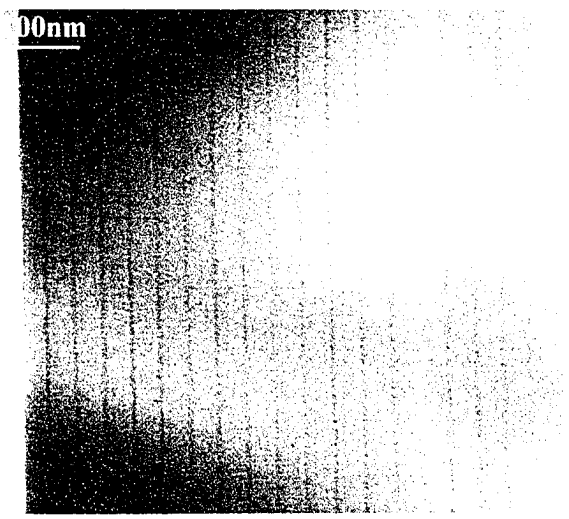


**(c)** Specimen S4, with eighteen nc-Si layers each 10 nm thick. The fifth layer from the substrate shows weaker contrast, reflecting some variation in the deposition parameters in this layer

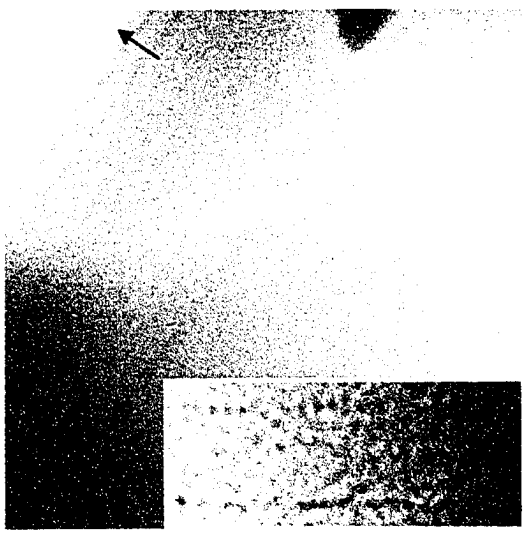

**(d)** Specimen S5. These ultra-thin nc-Si layers are difficult to observe and are shown in a magnified view in the inset. There are ten layers present, each 4 nm thick.

**Table 3.1:** Mean particle diameter values for specimens S1 through S4 (from a data set of between 200 and 300 particles for each specimen). Individual particle sizes were measured from TEM images. The mean particle diameter and standard deviation were calculated from the measured data.

| Specimen | Mean particle diameter (nm) Standard deviation 0.6 nm | Standard deviation (nm) |
|---|---|---|
| S1 | 2.9 | 0.6 |
| S2 | 3.3 | 0.6 |
| S3 | 2.9 | 0.6 |
| S4 | 3.1 | 0.6 |

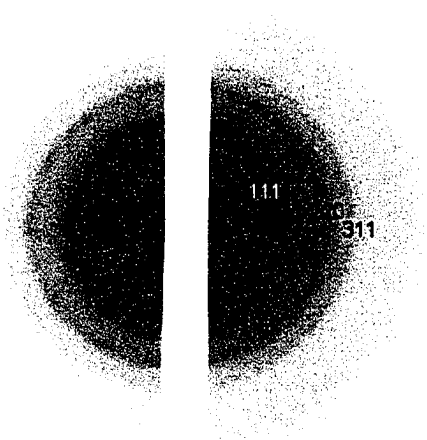


**Figure 3.5:** Electron diffraction pattern for the nanoparticles. Diffraction rings corresponding to the 111, 220, and 311 lattice planes of silicon are readily visible.

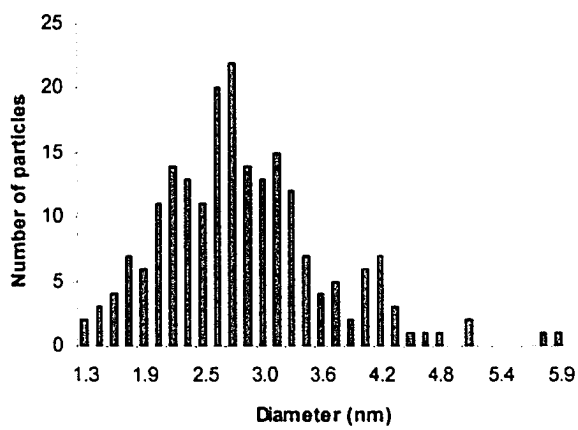


**Figure 3.6**: Size distribution of Si nanoparticles in specimen S1 with calculated mean diameter $d_{mean}$ and standard deviation $\sigma$ shown.

The composition of the active layers was found from energy dispersive X-ray analysis performed on specimen S1. A standard reference spectrum was taken from the fused quartz substrate and the SRO spectrum was taken from a nearby region of the film (see

diagram in Figure 3.7(a)). The spectrum from the SRO region is shown in Figure 3.7(b). The lowest energy peak (~0.5 keV) corresponds to the oxygen $k_\alpha$ line and the peak at ~1.8 keV corresponds to the silicon $k_\alpha$ line.

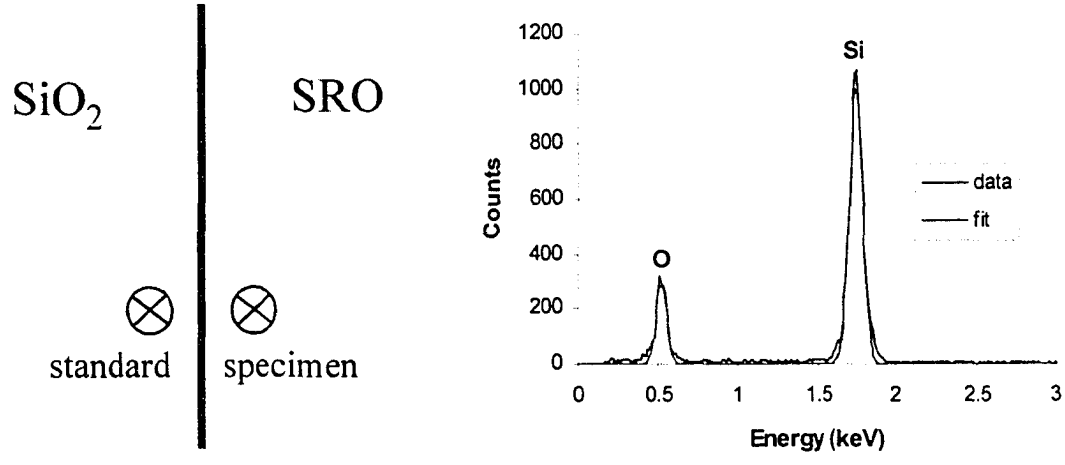


(a) (b)

**Figure 3.7**: **(a)** Diagram showing the location (indicated with a circled X) for energy dispersive X-ray measurements on specimen S1. The standard spectrum was measured in the quartz substrate, and the unknown spectrum was measured nearby in the SRO layer. **(b)** The energy dispersive X-ray spectrum of the SRO region showing the peaks corresponding to oxygen and silicon, and the non-linear least-squares fit to the data.

Although commercial software packages are available for calculating elemental concentrations from EDS data, I did not have access to such software. Instead, I used Matlab 6.1 to fit the EDS data using a standard non-linear fitting routine which used established background and peak fitting procedures. First, the standard spectrum from the quartz substrate was analyzed to determine a calibration constant that was then employed in calculations to determine the film composition. The standard spectrum was fit to the general formula:

$$N = N_B + N_O + N_{Si} \tag{3.1}$$

where $N$ is the counts as a function of energy, $N_B$ is the background function, and $N_O$ and $N_{Si}$ are Gaussians corresponding to the oxygen and silicon peaks, respectively. Each Gaussian has the form:

$$N_y = I_y \cdot e^{-\frac{\left(E - E_0^y\right)^2}{\sigma_y^2}} \tag{3.2}$$

where $I_y$, $E_0^y$, and $\sigma_y$ (the intensity, centroid, and width, respectively) are variables, and $y$ = O or Si, corresponding to oxygen or silicon.

The standard background function (Williams and Carter 1996) that was used is:

$$N_B = \left(\frac{a_0}{E} + a_1 + a_2 E\right)\left(1 - e^{-a_3 E}\right)^2 \tag{3.3}$$

where $E$ is the energy (in keV) and $a_0$, $a_1$, $a_2$, and $a_3$ are variables.

In this way, the integrated intensity of the oxygen peak and the silicon peak, $I_O$ and $I_{Si}$ from the standard (the $SiO_2$ substrate) was calculated. Although the atomic concentration of the standard is known, the ratio of the concentrations cannot be assumed to equal the ratio of measured X-ray intensities. Therefore, the standard is needed in order to find the correction factor $k_{SiO}$ in following the equation (Williams and Carter 1996)

$$\frac{C_{Si}}{C_O} = k_{SiO}\frac{I_{Si}}{I_O} \tag{3.4}$$

where $C_{Si}$ and $C_O$ are the atomic fractions of Si and O. This method is known as the "Cliff Lorimer ratio technique". Equation 3.4 can then be "re-used" for the unknown, by inserting the calculated k-factor and the measured intensities. However, there are still two

unknowns ($C_{Si}$ and $C_O$), so a second equation is needed to obtain the elemental compositions:

$$C_{Si} + C_O = 1 \tag{3.5}$$

This sets the total atomic fraction to unity. With equations 3.4 and 3.5 and the calculated k-factor, the elemental concentration of Si and O in the SRO layer can be obtained from the measured X-ray intensities. The resulting atomic concentrations were normalized to one silicon atom per formula unit. In this way, the SRO region was found to have a composition of $SiO_x$, where x = 1.2. This value is slightly different from the findings of Kahler and Hofmeister (2001), who obtained x close to 1.5 for evaporation of SiO in a similar oxygen pressure, presumably due to system differences (location of the sample with respect to the evaporant and the oxygen source, location of the pumping system, etc.). Nevertheless, as discussed in Section 3.3.1, the PL results are in reasonable agreement with the results of Kahler and Hofmeister (2001) for films of a similarly silicon-rich composition.

## 3.3 Absorption and Photoluminescence

### 3.3.1 X-series Results

Transmission spectra of the X-series specimens are shown in Figure 3.8 and can be directly compared with the photoluminescence spectra in Figure 3.9. Also shown is the transmission spectrum of a blank fused quartz ($SiO_2$) wafer. The substrate is transparent above approximately 250 nm. Silicon nanocrystals, however, absorb at shorter wavelengths. Specimens X1 and X2 absorb more than X3 and X4 due to the presence of more absorbing material (thicker $SiO_x$ layers). The slight oscillations in the transmission spectra

are the typical results of interference due to the refractive index contrast between the $SiO_2$ and $SiO_x$ layers. The refractive index of $SiO_2$ is approximately n = 1.41 to 1.53 in the ultraviolet to infrared range according to the commercial vendor of the fused quartz wafers (www.escoproducts.com). The refractive index of $SiO_x$ can be approximated by that of SiO as x is very close to 1. Ellispsometry data for SiO gives a value of n = 1.75 to 1.87 in the ultraviolet to infrared range.

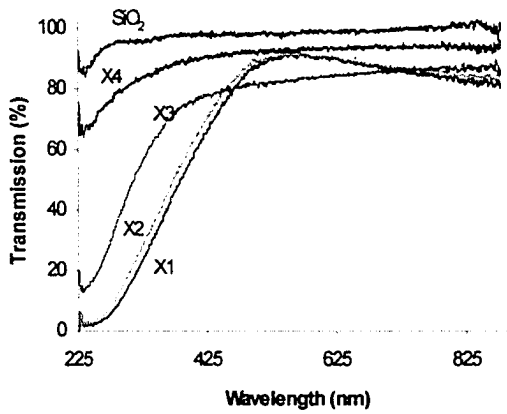


**Figure 3.8:** Transmission spectra of X-series specimens and of a blank fused quartz substrate (labelled $SiO_2$).

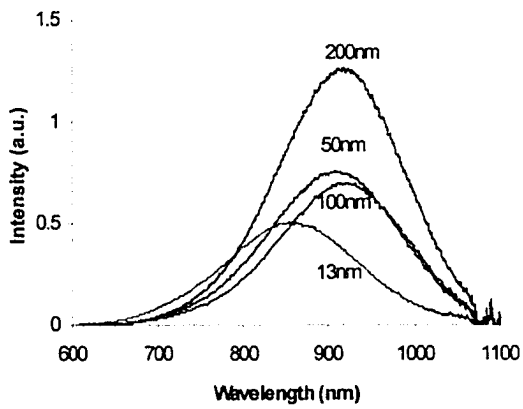


**Figure 3.9:** PL spectra of single-layer nc-Si films: specimens X1 (200 nm) to X4 (13 nm).

These are raw data - that is, there is no correction for the amount of luminescent material in the films. All the samples show a broad, featureless red-infrared luminescence band typical of silicon nanocrystal composites. There is a continuous blueshift of the peak emission wavelength for the thinner films and the full-width-at-half-maximum (FWHM), as estimated by peak fitting (see Section 4.1) decreases slightly (from 83 - 68 nm) for thinner films. The raw PL intensity does not show any regular trend and increases in the following order of film thickness: 13 nm - 100 nm - 50 nm - 200 nm.

Specimen X2 is 100 nm thick, like the specimens of Kahler and Hofmeister (2001) of which were prepared by the same methods used in this thesis. Since we did not measure

the composition or the nanoparticle size for the X-series specimens (and it probably differs some from the S-series specimens), we cannot compare specimen X2 extensively to the Kahler and Hofmeister specimens. We can note, however, that the Kahler and Hofmeister specimen with the lowest oxygen content ($SiO_x$ with x = 1.17) has its PL peak wavelength at 882 nm (more red-shifted than all their other specimens) which shows a general agreement with the PL of specimen X2 with its peak wavelength at 918 nm.

### 3.3.2 S-series Results

As for the X-series, transmission spectra of all S-series specimens were taken to provide information about changes in absorption that may occur, in addition to the information about the emission provided by PL spectra. Transmission spectra of the five S-series specimens are shown in Figure 3.10. In specimens S1-S4, the absorption onset occurs in the blue-green part of the spectrum. It is difficult to make direct estimates

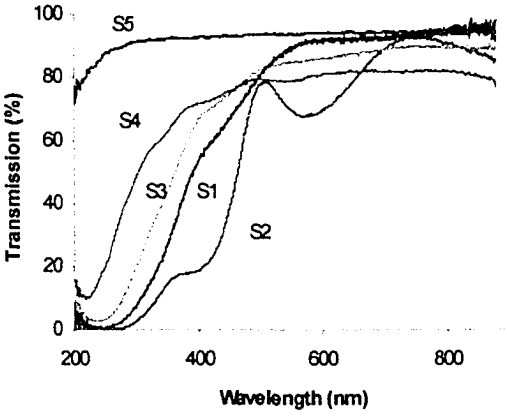


**Figure 3.10**: Transmission spectra of S-series specimens

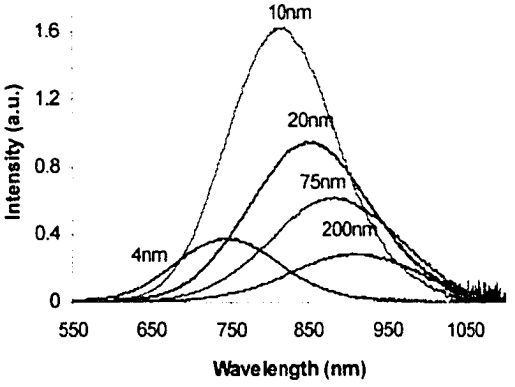


**Figure 3.11**: PL spectra of specimens S1 (200 nm nc-Si layer) to S5 (4 nm nc-Si layers).

because of the extensive oscillations in the spectra due to optical interference as a result of the refractive index contrast between the nc-Si and $SiO_2$ layers. The transmission spectrum of specimen S5 decreases weakly across the visible and the specimen only becomes

strongly absorbing in the UV. In this specimen, the layers are too thin (~4 nm) to observe interference oscillations. Standard matrix calculations were also undertaken using optical constants for SiO and $SiO_2$, and the simulated transmission spectra agreed quite well with the data.

The photoluminescence spectra taken from the samples in series S are shown in Figure 3.11. The PL intensity is not a direct indication of the efficiency of the photoluminescence, as each sample has a different total amount of silicon nanocrystal material (see Table 2.1). However, it can be observed that the PL peak blueshifts regularly as the nc-Si layers are made thinner, going from 911 nm for the 200-nm-thick single layer to 747 nm in the 4-nm-thick single layers. The intensity also increases regularly for the thinner layers, except for specimen S5. This is due to the small amount of luminescent material in that sample (40 nm total thickness). In this case, the full-width-half maximum of the broad PL peak decreases with decreasing layer thickness from 83 nm to 68 nm on going from S1 to S5.

Since the effect of layer thickness was so pronounced for these specimens, it was decided to compare the PL spectral shift to that obtained by varying the excitation wavelength. Varying the pump wavelength should selectively excite differently-sized nanoparticles due to the quantum confinement effect. Specimen S1 was excited with 325 nm, 442 nm, 456 nm, 476 nm, 488 nm, and 514 nm laser light, all at a CW power of 20 mW and with a similar laser spot size. As shown in Figure 3.12, the emission spectra have only a weak dependence on the excitation spectrum - with a change in excitation wavelength of over 200 nm, the PL peak was observed to shift only by ~14 nm.

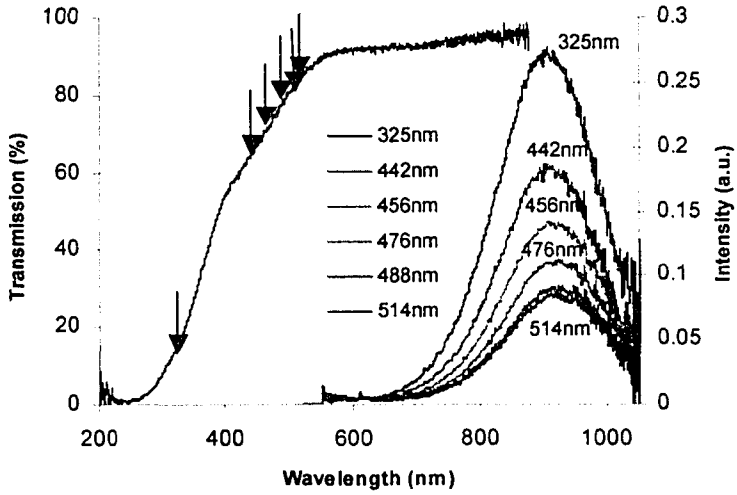


**Figure 3.12**: Transmission spectrum of S1, and PL spectra at six different excitation wavelengths (indicated on the transmission spectrum by arrows). The PL spectrum excited by 488 nm light is not labeled for clarity, but is directly above the one labeled 514 nm.

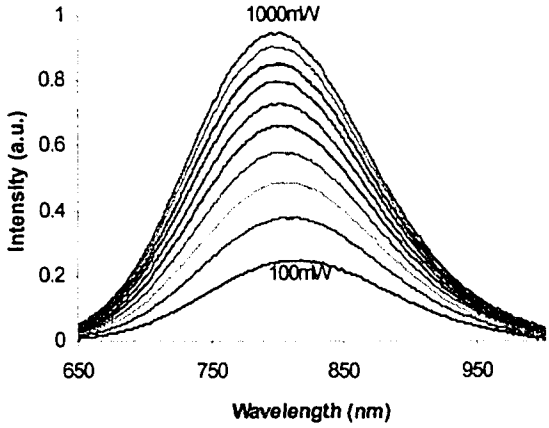


**Figure 3.13**: PL of specimen S4 using 488 nm excitation ranging in power from 100 mW to 1000 mW, in 100 mW increments.

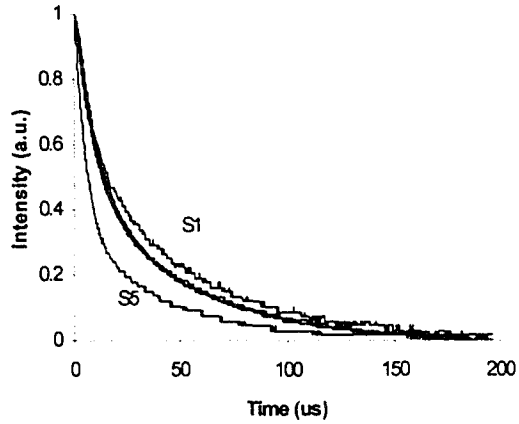


**Figure 3.14**: PL decay spectra, normalized to same initial intensity. The traces for S2, S3, and S4 are virtually indistinguishable.

Using 488 nm excitation, the change in the PL spectra when excitation power varied between 100 mW and 1000 mW was examined on all S-series specimens. Representative spectra from specimen S4 are shown in Figure 3.13. The trend is similar in all five

specimens. As excitation power is increased, the PL intensity increases, but gradually tends toward saturation. The PL peak blueshifts, but this shift also tends toward saturation at higher power. This observation is consistent with the PL pump-dependency that was previously observed by Hryciw *et al.* (2004).

The photoluminescence decay spectra for the S-series of specimens are shown in Figure 3.14. Specimen S5 exhibits the steepest intensity drop-off, and specimen S1 appears to have the longest lifetime. The PL decay traces of specimens S2, S3, and S4 overlap so that they are essentially indistinguishable. The spectra shown in Figure 3.14 are normalized to the same initial intensity. The initial intensity in un-normalized spectra followed the same trend shown in Figure 3.11 for the overall CW luminescence intensity. The pixelation seen in the spectra are due to the limited dynamic range of our 8-bit oscilloscope.

### 3.3.3 O-series Results

The transmission spectra of the O1- and O2-series are shown in Figure 3.15. The O1 series specimens are composed of four 20-nm-thick nanocrystal layers separated by 0, 5, 10, and 15 nm $SiO_2$ buffer layers (specimens O1a, O1b, O1c, and O1d, respectively). The O2 series was formed in the same way, except that the buffer layers were 0, 2, 4, and 6 nm thick (specimens O2a, O2b, O2c, and O2d, respectively). The transmission spectra are due to the different amounts of absorbing material in the different samples and to the effects of interference contrast between the film and the $SiO_2$ wafer, however the data are quite similar for both sample sets.

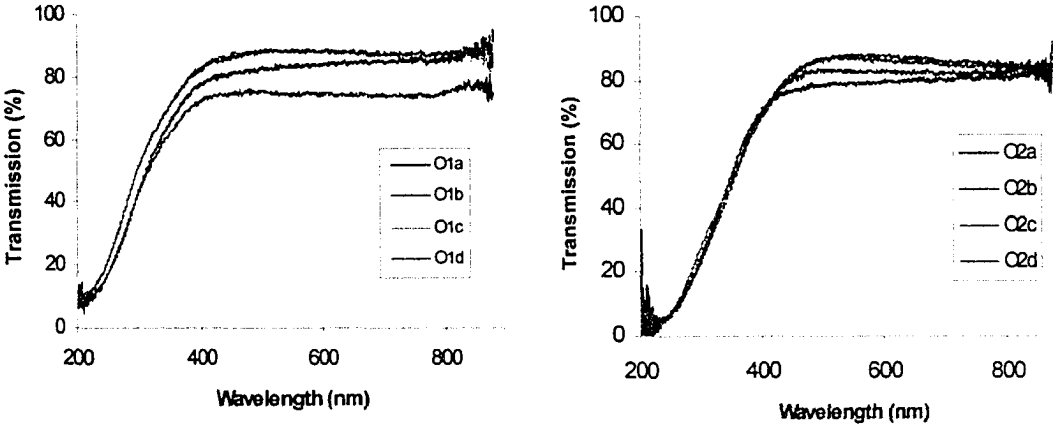


(a) (b)

**Figure 3.15:** Transmission spectra of **(a)** O1-series and **(b)** O2-series.

The photoluminescence spectra of specimens in the O1-series are shown in Figure 3.16. This was the first sample set prepared in which the effect of the buffer layer thickness was investigated. All samples have the same total amount of nc-Si material (80 nm), separated into four layers by buffer layers of various thicknesses. Specimens O1b, O1c, and O1d have approximately the same PL intensity. The PL spectrum blueshifts as the buffer layer thickness is increased, with the peak position changing by about 20 nm in total. There is only a slight difference in the PL peak wavelength among specimens O1b, O1c and O1d, which have buffer layers of 5, 10, and 15 nm, respectively. In this initial sample set, the effects of

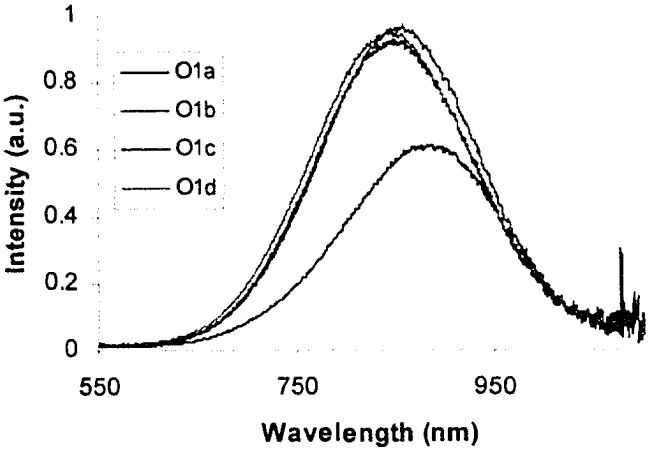


**Figure 3.16**: PL spectra of the O1-series specimens: 4 periods; 20 nm nc-Si layers separated by $SiO_2$ of a thickness ranging from 0 nm (O1a) to 15 nm (O1d).

the buffer layers appeared to saturate somewhere below a thickness of 10 nm. Therefore, a second set of samples was prepared (the O2 series) in which the buffer layers were thinner.

The PL spectra of the O2-series are shown in Figure 3.17. In this series, the buffer layers were only 2, 4, and 6 nm thick in order to try to better resolve the spectral evolution as a function of buffer thickness. Specimens O2a and O2b have approximately the same PL intensity and spectral shape (the spectrum of O2a is only slightly more intense than that of O2b). In this series, I again observed a blueshift and increasing intensity trend with increasing buffer thickness, although in this second sample set, it is not clear whether the effect has saturated. The magnitude of the blueshift in the O2-series is approximately a fifth of that in the O1-series. Both series are consistent in that the buffer effects probably saturate at an $SiO_2$ layer thickness close to 10 nm.

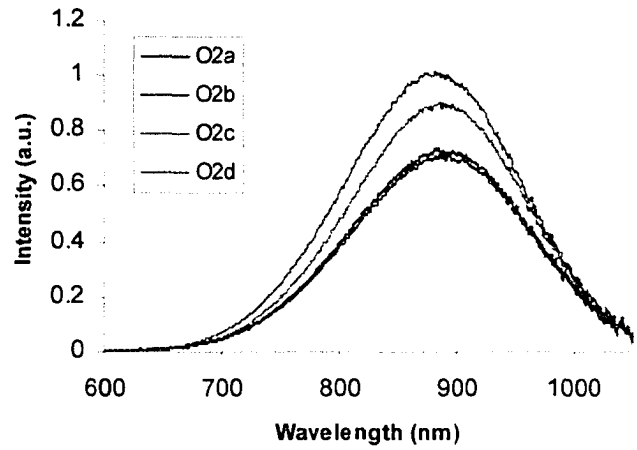


**Figure 3.17:** PL spectra of the O2-series specimens: 4 periods; 20 nm nc-Si layers separated by $SiO_2$ of a thickness ranging from 0 nm (O2a) to 6 nm (O2d).

### 3.3.4 E-series Results

Transmission spectra of specimens E1 (20 nm $Er_2O_3$ and 20 nm nc-Si layers) and E2 (1 nm $Er_2O_3$ and 20 nm nc-Si layers) are shown in Figure 3.18, along with a spectrum from a 200-nm-thick $Er_2O_3$ film prepared by electron beam evaporation in conditions

identical to the preparation of E1 and E2. The $Er_2O_3$ film exhibits strong interference oscillations. The absorption from the ground state to the $^4G_{11/2}$ and the $^2H_{11/2}$ levels can also be seen as small "dips" (marked by arrows) in the spectrum at wavelengths of approximately 370 nm and 525 nm, respectively. These are not observable in the multilayers because of the smaller total amount of $Er_2O_3$ in those specimens. Interference oscillations are observable in all three specimens but the effect is least evident in specimen E2.

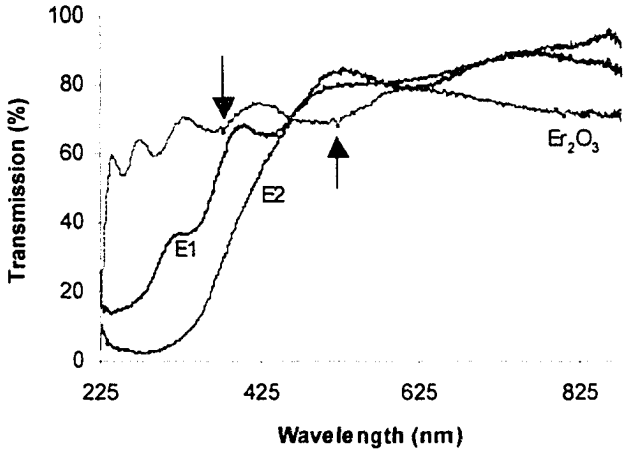


**Figure 3.18:** Transmission spectra of specimens E1, E2, and a 200-nm-thick $Er_2O_3$ film. Arrows indicate "dips" due to absorption from the ground state.

For the two specimens in the E-series, both the red-infrared emission of the Si nanocrystals and the infrared emission of the Er ions were investigated. The infrared portion of the PL spectra, excited at 500 mW, is shown in Figure 3.19. Resonant excitation uses 488 nm light, which corresponds to the transition from the $^4I_{15/2}$ ground state to the $^4F_{7/2}$ excited state in erbium. For non-resonant excitation, 476 nm light was used because it does not correspond to any possible erbium transition. Any erbium luminescence seen under non-resonant excitation must be due to carrier transfer from the nanocrystals (*i.e.*, the nanocrystal "sensitizing" effect - see Polman (1997)). Specimen E1, having the thicker

$Er_2O_3$ layers (20 nm), has rather weak erbium luminescence under non-resonant excitation. However, with resonant excitation it emits strongly at 1540 nm and 980 nm, due to the well-known transitions from the first and second excited states to the ground state of the $Er^{3+}$ ion. In the case of the thinner $Er_2O_3$ (specimen E2), there is little difference in the overall Er spectra for resonant and non-resonant excitation.

The broad nanocrystal PL shows some particularly interesting characteristics in specimens E1 and E2. In specimen E1 (20-nm-thick $Er_2O_3$ layers), the nanocrystal PL is almost completely quenched for excitation both resonant and non-resonant with erbium. However, in Specimen E2, the Si nanocrystal PL is slightly more intense for excitation resonant with erbium than it is for non-resonant excitation. Since resonant excitation is at a higher wavelength (488 nm) than the non-resonant excitation (476 nm), this is opposite to the trend in Figure 3.12 - that is, the nanocrystal PL is more intense for 488 nm pumping despite the lower absorption, as compared to that at 476 nm. This trend in PL intensity is opposite to that observed in the *absence* of the $Er_2O_3$ layers. I will come back to this point in the discussion; however, it is already clear that the $Er^{3+}$ ions, although in separate layers from the nanoparticles, have a pronounced effect on the nanocrystal PL (and entirely quench it in specimen E1).

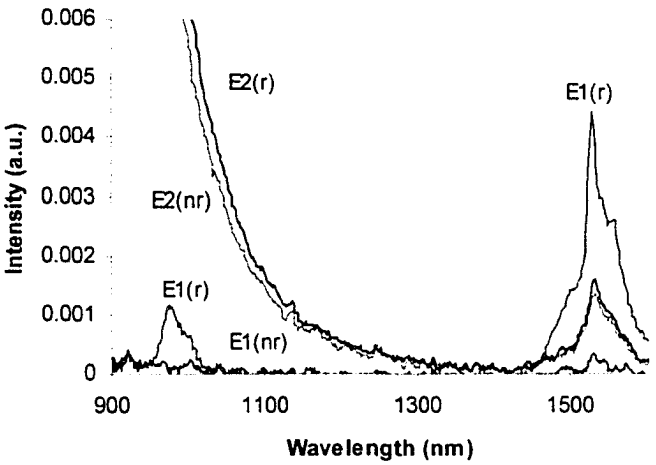


**Figure 3.19**: PL spectra for E1 (10 periods: 20 nm nc-Si and 20 nm $Er_2O_3$) and E2 (10 periods: 20 nm nc-Si and 1 nm $Er_2O_3$). (r) corresponds to resonant (488 nm) excitation and (nr) to non-resonant (476 nm) excitation. The laser power was 500 mW.

# Chapter 4: Discussion

The results presented in Chapter 3 show that the PL peak wavelength shifts with nc-Si-layer thickness, as will be discussed below. The observed change in PL intensity with active layer thickness cannot be explained by the lowering of the radiative state energy predicted by the "reactive nanocluster" model. It will be shown in this chapter that the experimental evidence points toward carrier migration between slightly separated nanocrystals, and an "interactive nanocluster" model will be introduced. This thesis presents a fairly large amount of experimental data and there were some techniques that could be applied to this data that have not been attempted (for example, one could imagine using rate equations to model the lifetimes of the nanoparticles and the erbium, or one could study in detail the oscillations in the transmission spectra). For this thesis, I concentrated extensively on the interactive nanocluster model and on obtaining results that could more directly prove its applicability.

## 4.1 Photoluminescence Spectral Shift: The Effect of Layer Thickness

To examine the trend of the PL spectral shifts, the peak wavelength of each spectrum was determined from a least-squares fit of a Gaussian curve to the PL peak (see Figure 4.1). In fitting the PL spectra, the goal was to obtain the best possible estimate of the peak wavelength, since determining the peak by visual estimation seemed rather arbitrary. The Gaussian form was found to give the best fits (best residuals). Fits of a lognorm function were also attempted; however they resulted in worse fits with larger residuals. The deviation from the Gaussian form at the peak tail-ends resulted in a less-than-ideal peak fit. To correct this, only the middle portion of the PL peak, spanning approximately 200 nm, was fit (see inset of Figure 4.1). The PL peak wavelength and FWHM parameters

were obtained from these "central" fits (see Appendix for values from all fits). Nevertheless, the excellent fit throughout most of the curve means that the peak wavelength obtained by the curve fitting method should be more consistent than simple visual estimation.

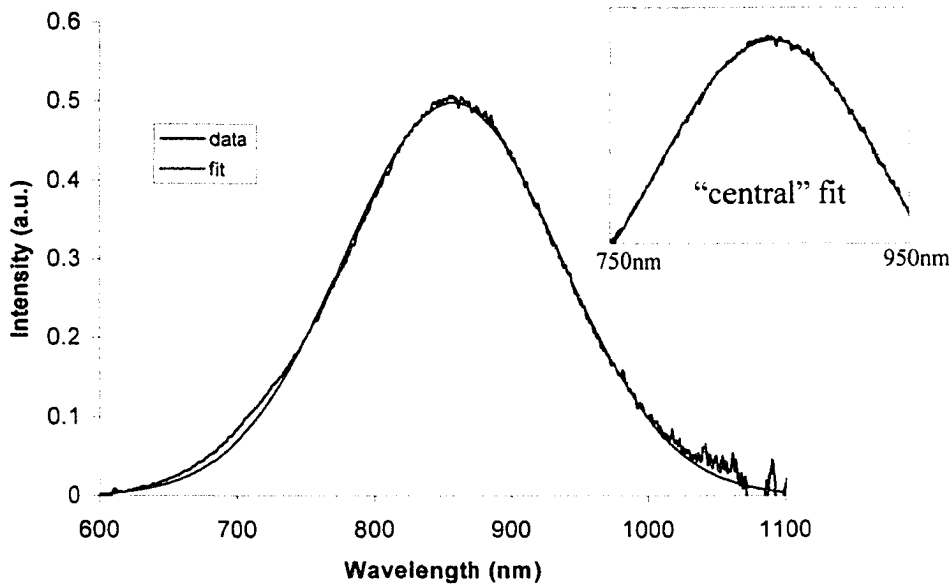


**Figure 4.1:** Least-squares Gaussian fit (the pink line) to the data for specimen X4 (blue line). The fit in the central region of the PL spectrum is shown in the inset.

In the X-series and the S-series, the PL peak wavelength blueshifts as nc-Si layer thickness decreases as shown in Figure 4.2. The first question is: why is the light emission of nanoparticles in thick layers less energetic than that of nanoparticles in thin layers? The spectral blueshift with decreasing nc-Si layer thickness is not within the direct scope of the reactive nanocluster model of Iwayama *et al.* (1998; 1999; 2000), since the average particle spacing *should not change* in the different samples. The TEM results (and the overall similarity in the preparation methods) show that the size and spacing of the particles remains consistent - the only variable is the thickness of the various layers. Stated simply,

there is no obvious parameter (*i.e.*, the interparticle spacing) in the reactive nanocluster model that changes in my samples. The main sample-to-sample difference is the fraction of nanocrystals located adjacent to a buffer layer (as well as, in the O-series samples, the thickness of the buffer). Therefore, it seems that carrier migration effects must be considered in an evaluation of the PL results, at least when the particles are closely spaced.

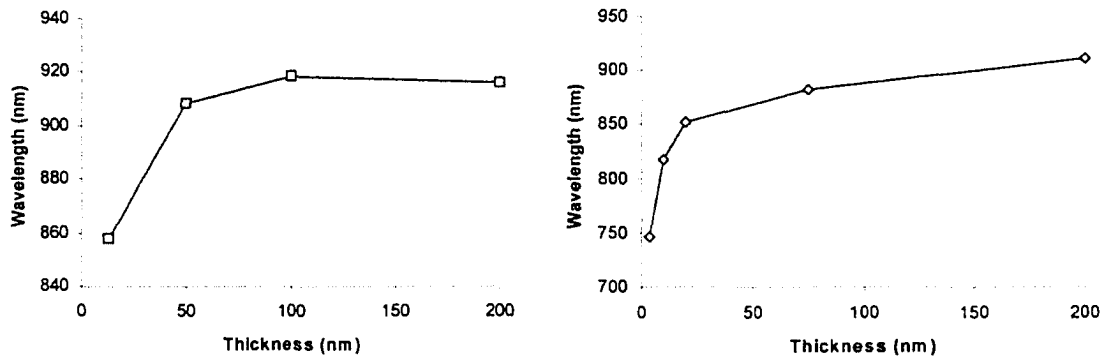


**(a)** **(b)**

**Figure 4.2:** The change of PL peak wavelength with increasing nc-Si thickness for **(a)** the X-series specimens and **(b)** the S-series specimens. The peak wavelength was determined from a non-linear least-squares fit of a Gaussian to each PL spectrum.

Although the reactive nanocluster model can accommodate a PL spectral shift, it requires a difference in the separation between adjacent nanoclusters. As such, we believe that the PL spectral shift is the result of carrier *migration*. If charge carriers leave one nanoparticle to migrate to another, they should preferentially move to a state of lower energy, resulting in an overall redshift of the emission spectrum. In fact, carrier migration has already been evoked as an explanation for a PL redshift by Cheylan and Elliman (1999). They studied the PL spectra of nc-Si samples with varying Si concentrations. Samples with higher Si concentrations (*i.e.*, more closely-spaced nanoparticles) had PL spectra redshifted relative to those of lower concentration samples. The redshift was attributed to carriers migrating from small particles (high energy) to large particles (low

energy), with emission being across the bandgap. In that paper, however, it was difficult to isolate the effects of nanocrystal spacing from nanocrystal size due to the variable composition of the different specimens investigated. Furthermore, possible effects of the radiative center (now widely recognized as being a critical factor in the luminescence) were not considered. My results will be shown below to require a sub-gap state *in addition* to carrier migration.

Nevertheless, there may still be some arguments in favor of the reactive nanocluster model, in the sense that the geometric isolation of surface states on a nanocrystal bordering a buffer layer may not undergo energy lowering and contribute to the observed spectral blueshift in thinner layers. Certainly, thin nc-Si layers have a large fraction of their nanoparticles on the layer surface, where there are fewer neighbouring particles. This argument would imply some form of geometric consideration in the reactive nanocluster model; however, I will show below that the reactive nanocluster model also fails to explain the observed intensity variations.

## 4.2 Effects of Layer Thickness On Emission Intensity

From inspection of Figures 3.9 and 3.11, it appears that the specimens with thinner nc-Si layers in the X- and S-series are more efficient emitters than the thicker nc-Si layers. To examine this trend in a more quantitative manner, each PL spectrum of the X- and S-series specimens was scaled according to its the total amount of nc-Si material (by dividing the spectrum by the total thickness). The resulting spectra, shown in Figure 4.3, are now a more accurate indicator of the relative emission efficiency in the different samples.

The reactive nanocluster model, with its lowering of the radiative energy due to interaction with neighbouring nanoparticles, cannot explain this PL intensity change.

Iwayama *et al.* (1998) do mention that "interactions" can cause a change in the PL intensity, but they do not provide any speculation about what these interactions may be. However, the increase in PL intensity with decreasing nc-Si layer thickness makes sense if one considers the possibility of carriers "flowing" (*i.e.*, migrating) throughout the nc-Si layer.

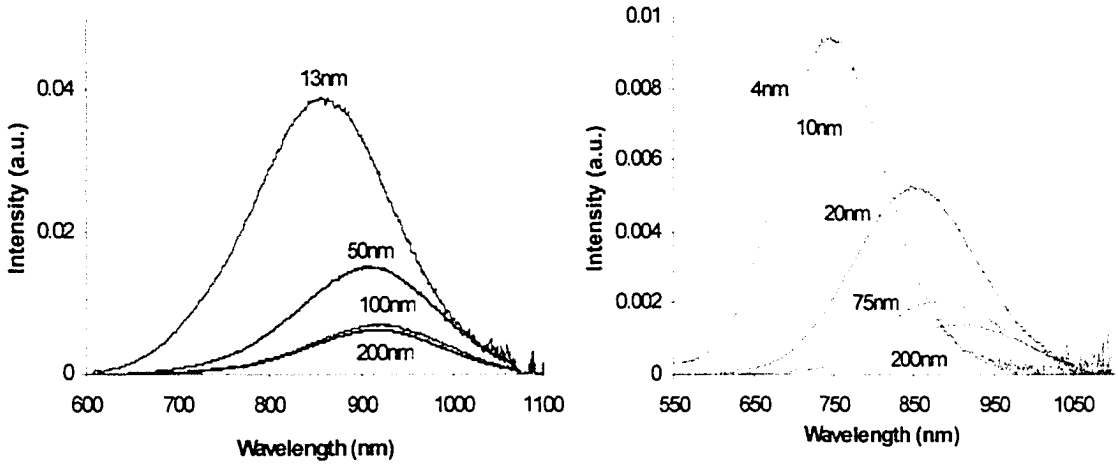


**Figure 4.3: (a)** PL spectra of X-series specimens (single layer nc-Si films), scaled by their total thickness (labelled). **(b)** PL spectra of S-series specimens (multilayered specimens), scaled by the total nc-Si thickness (labelled).

If carriers (most likely electrons, as discussed below) can migrate, then one obtains a situation in which non-radiative centers can be more important. In completely isolated nanoparticles, a non-radiative center (*e.g.*, an unpassivated silicon dangling bond, as discussed in Section 1.2.2) would only be able to quench the nanoparticle in which it resides. If charges can migrate, however, a non-radia-

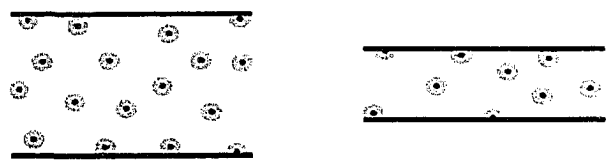

**(a)** **(b)**

**Figure 4.4**: Non-radiative centers (black circles) and their capture areas (grey areas) in two-dimensional nc-Si layers, bounded by layers of oxide. Specimen (a) is a single nc-Si layer twice as thick as specimen (b), but with the same number of randomly scattered defects per unit area. Due to the limited vertical dimension in (b), some of the full circles in this two dimensional picture are "cut off" by the surface, resulting in a smaller net quenchable area (per total area) in the thinner layers. The same analysis, of course, applies in three dimensions.

tive center can potentially affect a surrounding volume containing many particles. Therefore, carrier migration would have two effects: a luminescence redshift (as discussed above) and decreased intensity due to the effect of non-radiative centers - exactly as observed in the present specimens. Non-radiative centers located on nanoparticles adjacent to a buffer layer (at the nc-Si/$SiO_2$ interface) will have fewer neighbours than their counterparts inside the layer, and therefore the volume of material that can be affected by a non-radiative center is smaller (see Figure 4.4).

The O-series of samples shows that the SRO layers become effectively isolated above a buffer separation of 5-10 nm (as will be discussed in Section 4.5.2). Therefore, the SRO layers in the S-series specimens can be considered isolated, with each layer adding to the overall intensity but not "communicating" with the others. The X-series shows that the normalized intensity decreases as the active layer gets thicker, but this effect appears to saturate at thicknesses between 100-200 nm. This probably occurs because the fraction of surface particles is insignificant at these layer thicknesses, so that there is no significant change in the capture volume available to flowing charge carriers.

## 4.3 Effect of Particle Size

The effect of excitation wavelength on the PL integrated intensity and PL peak wavelength is shown in Figure 4.5. This is a type of rough photoluminescence excitation (PLE) experiment in which shorter pump wavelengths are used to excite the smaller nanoparticles. In the pure quantum confinement theory, exciting smaller particles (via a shorter pump wavelength) should also result in a blueshift of the emission spectrum.

As can be seen from Figure 4.5(b), the fractional change in the PL intensity of specimen S1 (variation by a factor of ~4) is much larger than the fractional change in the

PL peak wavelength, which varies only by a few nanometers. This is true for all the S-series specimens. The intensity increase at least roughly follows the increase in absorption (Figure 4.6). It is difficult to ascertain from this data whether the relationship is linear. An exponential least-squares fit does give the lowest residuals, which may suggest a slightly increasing quantum efficiency for smaller particles. In any case, there is clearly a monotonic relationship between pump absorption at different wavelengths and emission intensity, but there is only an extremely weak relationship between pump wavelength and the PL spectrum.

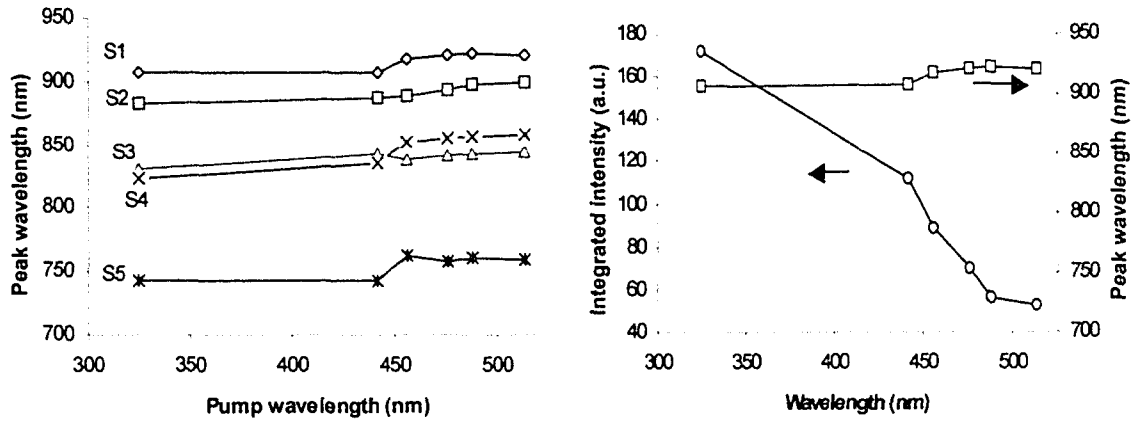


**(a)** **(b)**

**Figure 4.5: (a)** The shift of the PL peak wavelength for the S-series specimens as the pump wavelength is varied. **(b)** Pump wavelength dependence of S1 PL peak integrated intensity and peak wavelength. The vertical scale is the same as that of Figure 4.2(b). Notice that the PL peak shift is much smaller when the pump wavelength is varied (this figure) as compared when the layer thickness is varied (Figure 4.2(b)).

The pump photon energy employed in the present experiments ranged from 3.81 eV to 2.41 eV. According to Delerue *et al.* (1999), this corresponds to particles with diameters ranging from 0.9 to 2.7 nm. The emission should, therefore, blueshift accordingly in the pure quantum confinement model (minus relatively small Coulomb and spin interactions). In contrast, these samples have Stoke shifts ranging from approximately 0.85 eV to 1.77 eV in the different specimens and a PL peak shift of only ~20 meV over a 1.4 eV

shift in the pump energy. This combination of observations makes it difficult to defend a pure quantum confinement model with these data.

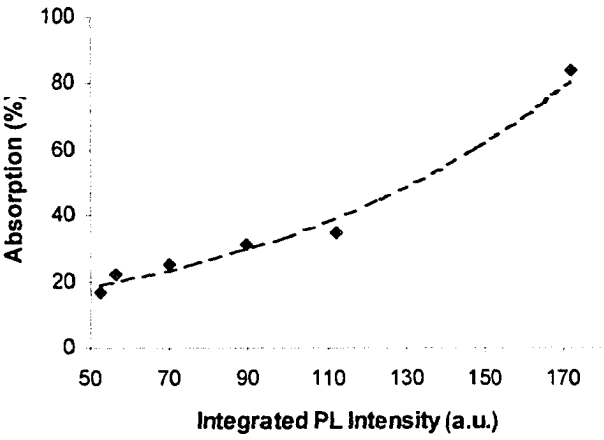


**Figure 4.6:** Absorption at six different excitation wavelengths (as shown in Figure 3.12) as a function of the integrated PL intensity of specimen S1.

Nevertheless, there seems to be a minor correlation between nanoparticle size and the energy of the radiative surface state, as observed in the monotonic shift (by 14 nm) in the peak wavelength for different excitation wavelengths. The exact nature of this correlation is unclear. Several models have been proposed in which the energy of the radiative centers tracks the bandgap energy (*e.g.*, Vasiliev *et al.* 2002), so that smaller nanoparticles do emit shorter wavelengths, but not as short as they would in the absence of the Si=O bond. This may be consistent with the present results, in which there is a very small but consistent blueshift for shorter pump wavelengths, although even the model of Vasiliev et al. (2002) predicts larger PL shifts than we observe. Therefore, the results presented in this thesis seem impossible to reconcile with the pure quantum confinement model, do not fit models involving radiative centers only (*i.e.*, without additional mechanisms), and cannot be explained by the reactive nanocluster model only.

To recap, the emission spectrum shows little dependence on particle size, but is instead dominated by the thickness of the nc-Si layer, as discussed in Section 4.2. All specimens in each series were prepared identically, so the particle size distribution was as similar as possible for all specimens in a series, as confirmed by TEM images of the S-series specimens. Particle size has therefore been eliminated as a variable in the four sets of samples grown in this work. By using variable pump wavelengths, one can, however, effectively obtain size selection *within the same sample*. The spectral results show little or no direct dependence on the pump wavelength (although there is a strong intensity dependence due to increased absorption at shorter wavelengths). Finally, none of the models discussed above adequately describes the data.

## 4.4 Excitation Lifetime in Silicon Nanocrystals: Effect of Layer Thickness

The PL lifetime results for the S-series (Figure 3.14) were fitted using a non-linear least-squares routine. The data were fit to a single exponential decay (intensity and lifetime as free parameters), a sum of two single exponential decays, and a stretched exponential (intensity, lifetime, and exponent as free parameters). For each specimen, the stretched exponential form gave the best fit (lowest residuals). The fitted parameters $\tau$ and $\beta$ are shown in Fig-

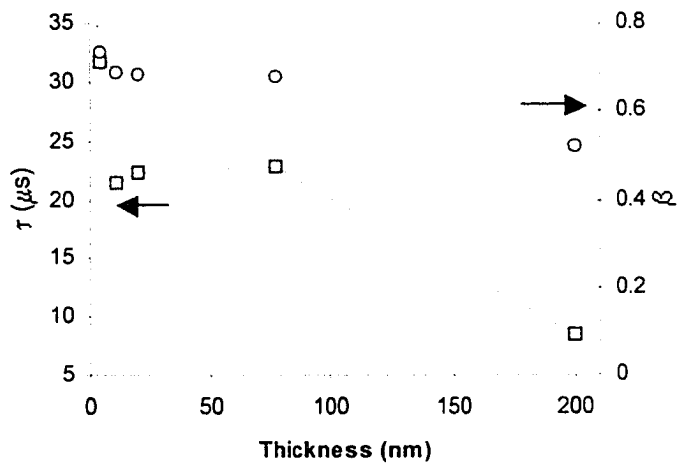


**Figure 4.7**: PL lifetime ($\tau$) and exponent ($\beta$) from the stretched exponential function fit to the PL intensity decay spectra of S-series specimens.

ure 4.7. The lifetimes range from ~9 to 31 $\mu$s and $\beta$ lies between 0.5 and 0.8. The lifetimes and exponents for specimens S2 (75 nm), S3 (20 nm), and S4 (10 nm) are very similar. Specimen S1 (thickest nanocrystal layer) was observed to give the shortest lifetime and the lowest value for $\beta$, and specimen S5 (thinnest layers) has the longest lifetime and the highest $\beta$.

The values of $\beta$ and $\tau$ are, in general, consistent with models involving interactions between nanoparticles. For example, the PL lifetimes trend downward as the layer thickness increases - an observation that can be interpreted in terms of non-radiative decay processes. Similar to the argument discussed in Section 4.2, if carriers are mobile and long-lived then non-radiative traps can have large capture cross sections. Dividing the nanocrystal layers more finely implies more limited migration in one direction at least, so the effect of non-radiative traps is smaller when the layers are more separated. This will result in longer overall lifetimes in thinner layers (as observed), as well as increased intensity (also observed). Therefore, it is possible to ascribe the high values of $\tau$ and the increased intensity in the thinner specimens to the effects of carrier mobility and non-radiative trapping.

Further evidence can be obtained from the "stretching parameter" $\beta$. The stretching of the exponential decay spectrum is widely thought to be related to disorder (Pavesi 1996; Vial *et al.* 1992; Mihalescu *et al.* 1996). Therefore, according to this well-established hypothesis, more efficient carrier migration should lead to lower values of $\beta$ (Pavesi 1996). A thick layer provides, on average, more nearby nanocrystals for any given nanocrystal to interact with, which should lead to more migration possibilities and more

disorder within the specimen. It is interesting to note that even in specimen S5, which the TEM images showed to be a single plane of nanocrystals, the spectrum is still "stretched" (although less so than the other samples). This suggests that there are interactions within the plane that contribute to the overall disorder, which is consistent with the idea that the nanocrystals, while widely spaced parallel to the sample normal, are closely spaced (presumably to the degree where they can interact) within-plane. Others (Iacona *et al.* 2001b) have observed single exponential decays ($\beta = 1$) in single planes of nanocrystals, but the interparticle spacing may have been greater in that case.

Changing the excitation power is a qualitative way to examine the lifetime of Si nanoparticles. When the pump power is increased, the rate at which nanoparticles are

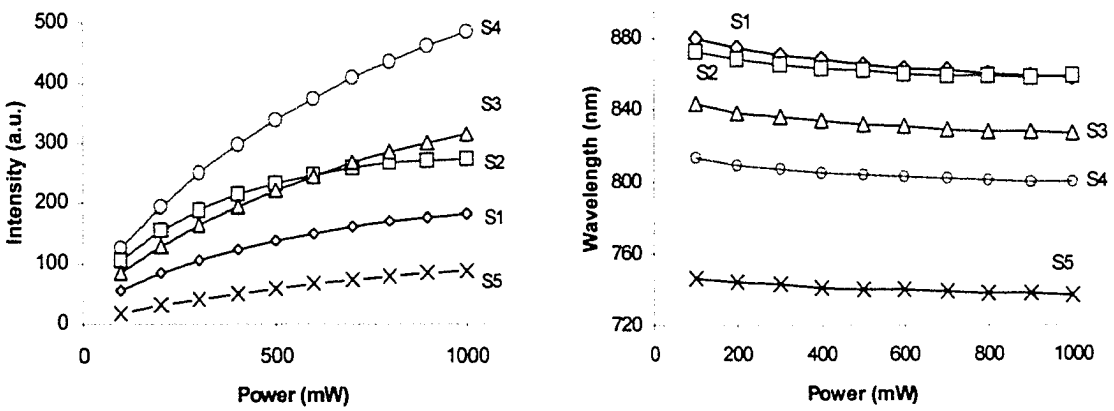


**(a)** **(b)**

**Figure 4.8:** Power dependence of **(a)** integrated intensity of PL peak and of **(b)** PL peak wavelength of S-series specimens.

excited is increased. Figure 4.8 shows the power dependence of the PL intensity and the PL peak wavelength for the S-series. The fact that the PL peak wavelength blueshifts with increasing power indicates that nanoparticles with lower energy radiating states saturate first, and thus have longer lifetimes than those having higher energy radiative states. Figure 4.9, which shows the power dependence of the specimen S4 PL intensity at 750 nm

(the high energy side of the PL peak) and at 850 nm (the low energy side) also confirms that lower energy radiating states saturate first, as the PL intensity at 850 nm approaches saturation before the intensity at 750 nm. This observation is consistent with many previous findings for both nanocrystals and porous silicon (*e.g.*, see Linnros *et al.* (1999)). Vinciguerra *et al.* (2000) found smaller particles to have faster dynamics - although in that case the spectral shift was attributed to particle size, which the present work has already shown to have only a limited effect on the emission of silicon nanoparticles, as compared to the particle spacing. In fact, Hryciw *et al.* (2004) found that the lifetime could be longer for samples with smaller particles, indicating that the wavelength dependence of the lifetime may not be directly related to particle size. Thus, these results do not affirm that small particles decay faster, as other authors have claimed. All that can be safely stated is that shorter wavelengths have shorter lifetimes, but as has been shown in Section 4.3, there is no straightforward and direct correlation of the emission spectrum with particle size. At present, however, we do not have the equipment needed for wavelength-dependent lifetime measurements, so we cannot confirm the results of others beyond the qualitative analysis of the pump wavelength dependencies.

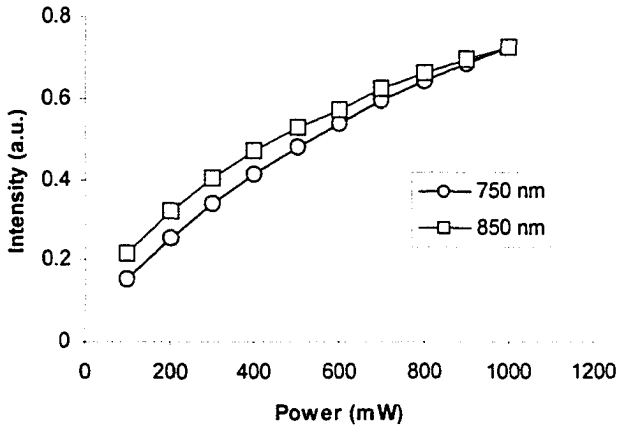


**Figure 4.9:** Power dependence of PL intensity at a wavelength on the high energy side of the PL peak (750 nm) and at a wavelength on the low energy side of the PL peak (850 nm) for specimen S4.

There are several competing processes that contribute to the observed lifetime. These processes can be radiative and non-radiative (in fact, non-radiative processes often dominate the fluorescence lifetime effects in silicon nanoparticles; *e.g.*, Vinciguerra *et al.* (2000)). Therefore, in the S-series, the specimen with the thinnest layers might be expected to have the longest lifetimes due to the relative "slowness" of non-radiative processes in that sample; but this effect might be offset to some degree by the naturally blue-shifted emission observed under identical pumping of thinner layers (bluer emission has shorter lifetimes). Clearly, this second effect is not enough to reverse the trend (the thinnest layers *do* have the longest lifetime in the S series specimens). The observations suggest that non-radiative lifetimes *increase* in ultra-thin nanocrystal layers but radiative lifetimes might *decrease* (although the latter effect would be smaller, giving an overall longer lifetime).

## 4.5 Carrier Migration Across Buffer Layers

### 4.5.1 $Er_2O_3$ Buffer Layers

The presence of non-resonant nanocrystal PL in Figure 3.19 shows that carriers are migrating from the silicon nanocrystal layer (where the excitation occurs) to the Er ions. The 20-nm-thick $Er_2O_3$ layers in specimen E1 fully quench the nanocrystal PL. This is significant, since it implies that the entire 20-nm-thick nanocrystal layer is affected by the presence of the nearby $Er_2O_3$. The clear implication is that carriers must be migrating through distances of over at least 10 nm (the distance from nanocrystals in the middle of the nc-Si layer to the edge of the $Er_2O_3$ layer). Furthermore, the $Er_2O_3$ emits characteristic radiation under *non-resonant* excitation conditions, clearly showing that the $Er^{3+}$ ions are

being excited via transfer from nanocrystals in the adjacent layers. In specimen E2, however, the nanocrystal PL is not entirely quenched. This specimen contains extremely thin layers (~1 nm) of $Er_2O_3$, so there may not be enough $Er^{3+}$ sites to take full advantage of the carrier transfer from the silicon nanoparticles. Therefore, nanocrystal fluorescence is observed, although it was weaker than for equivalent active layers with $SiO_2$ buffers (as opposed to the $Er_2O_3$ buffers in specimens E1 and E2).

A comparison of the relative intensities of the erbium emission under resonant or non-resonant excitation conditions is somewhat beyond the scope of this thesis, however a few qualitative comments can be made. Specimen E2 has a resonant erbium PL intensity that is approximately 1/3 that of specimen E1 (see Figure 3.19), despite the fact that E2 has ~1/20 the total amount of $Er_2O_3$ as compared to specimen E1. Specimen E2 is a more efficient emitter than E1 and the difference in efficiency may be due to the well-known concentration quenching effects that occur when Er ions are close together. In specimen E2, cooperative effects between Er ions should be more restricted in the vertical direction. In this sense, the difference may mirror what is observed in the nanocrystalline layers: for thinner $Er_2O_3$ layers, the intensity is brighter on a per material basis due to the limited carrier migration in the vertically confined layers.

Figure 4.10 shows the power dependence of the nanocrystal PL intensity of specimen E2 for both resonant and non-resonant excitation. As seen in Figure 3.19, at 500 mW excitation power, the nanocrystal PL of specimen E2 is more intense for the 488 nm pump than for the 476 nm pump. Since Si nanocrystal are less absorbing at 488 nm than at 476 nm, this difference seems at first to be counterintuitive. However, the intensity of the

nanocrystal luminescence is due not only to the pump power and wavelength, but also to the availability of erbium sites for carrier transfer. It was hypothesized that the reverse order of intensities may be due to the availability of erbium. For 488 nm excitation, both the nanocrystals and the Er are excited by the pump beam. Therefore, there would be fewer Er atoms available to accept carriers from the nanoparticles, leading to more intense nanocrystal PL for 488 nm (resonant with Er) excitation.

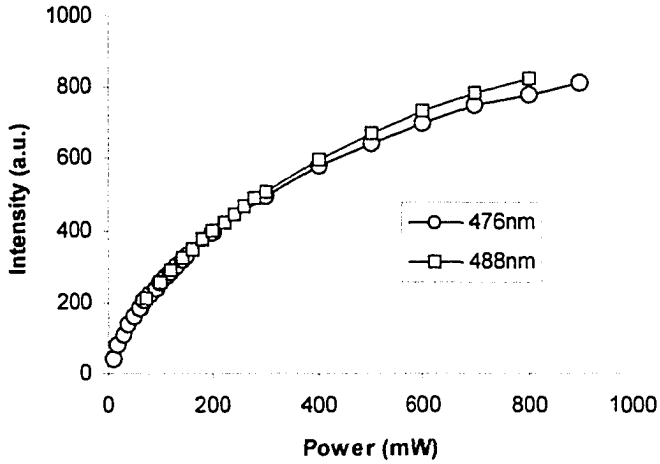


**Figure 4.10:** Power dependence of nanocrystal PL intensity for specimen E2 at non-resonant and resonant excitation.

In order to further test this hypothesis, the integrated intensity of the nanocrystal PL in specimen E2 was investigated as a function of 476 nm and 488 nm pump power. Looking at Figure 4.10, one can see that while the 488-nm-pumped PL is more intense at higher pump powers, the 476-nm-excited PL is more intense at low powers. In effect, there is a crossover at approximately 100 mW. This is also evidence in favour of carrier migration. Resonant (488 nm) pumping excites Er ions in addition to nanocrystals, making some Er ions unavailable to accept carriers from the Si nanoparticles. Then silicon nanoparticles cannot transfer carriers to the Er ions as effectively and the overall PL from the nanocrystal layer is more intense as a result. As the flux increases, this effect is enhanced as more of the Er ions are directly excited.

The power dependence of both the nanocrystal and erbium PL, for resonant and non-resonant excitation, for the E-series specimens is shown in Figure 4.11. These pump power dependencies are a reflection of the excitation rates for $Er^{3+}$ and Si nanocrystals, the rate of carrier migration in the nc-Si layers, and the rates of radiative and non-radiative decay for both Er ions and nanocrystals. I did not attempt rate equation modeling in this thesis, since these multilayer samples are complex and would require rate constants for carrier trapping, carrier migration, and carrier recombination in both nanocrystals and

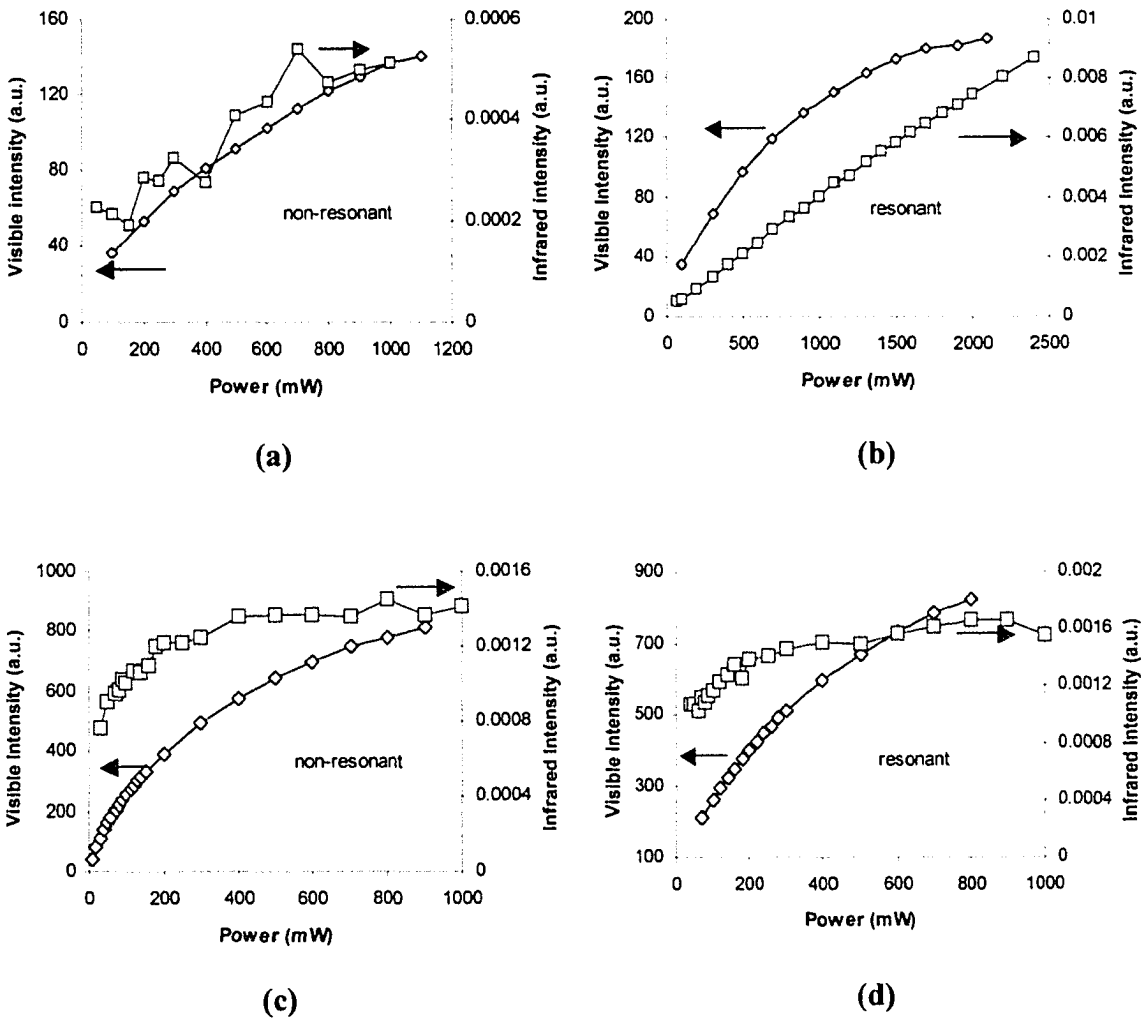


**Figure 4.11:** Power dependence of integrated nanocrystal PL intensity ("visible") and power dependence of erbium PL intensity ("infrared") at the emission wavelength: for specimen E1 excited **(a)** non-resonantly and **(b)** resonantly, and for specimen E2 excited **(c)** non-resonantly and **(d)** resonantly. The absolute values of the PL intensities cannot be compared directly to each other, but trends may be compared.

erbium ions (basically, there are so many unknowns that it was felt that model fits would have too many free parameters to produce really meaningful results in a realistic time frame). Nevertheless, examination of Figure 4.11 is still instructive. Figure 4.11(a) shows that non-resonantly exciting specimen E1 results in similar trends for both the Er PL and the nc-Si PL as they approach saturation, although the Er PL data are noisy. This seems reasonable given that the Er PL depends on the excitation of the nanocrystals. The resonantly-excited specimen E1 (Figure 4.11(b)) shows that the Er PL is linear over the range of powers investigated, while the nanocrystal PL goes toward saturation.There are so many Er ions to excite that increasing the power simply increases the number of excited Er ions, whereas the nanocrystals (despite there being as many nanocrystals as Er ions) are saturated at the highest powers. In Figure 4.11(c), we see saturation trends for both Er and nanocrystal PL, and the Er PL seems to be reasonably saturated by 400-500 mW, probably as a result of there being so few Er ions (only 1-nm-thick layers) in specimen E2 to receive transfers from the non-resonantly-excited nanocrystals. The Er ions of specimen E2 are once again easily saturated, this time by resonant excitation, and the nanocrystal PL does not tend to saturation as fast as it did in Figure 4.11(c), as the Er ions are being excited directly in this instance.

### 4.5.2 $SiO_2$ Buffer Layers

The E-series luminescence suggests that carriers can migrate among particles, and the combined migration distance can be as large as 10 nm or more in these specimens. The TEM results show that the nanocrystals are quite close together (although it is difficult to obtain exact estimates of the "average" interparticle spacing, a rough value of approximately 3 nm seems not unreasonable based on a visual inspection of the TEM images).

Since these specimens are fairly densely packed with nanoparticles, an obvious question has to do with the migration mechanisms and the distances over which the effect can occur. In other words, how far apart should these silicon nanocrystals be before they can be considered isolated?

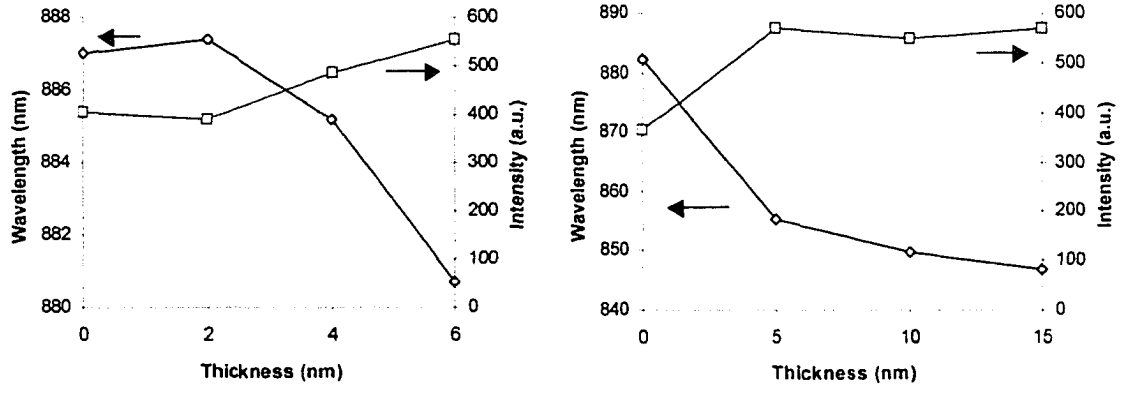


**(a)** **(b)**

**Figure 4.12:** The PL peak wavelength shift and integrated intensity change with $SiO_2$ thickness for **(a)** the O2-series specimens and **(b)** the O1-series specimens. The peak wavelength was determined from a non-linear least-squares fit of a Gaussian to each PL spectrum.

The O1-series and O2-series shed some light on this question. In Figures 3.16 and 3.17 we saw that the PL peak wavelength shifts to higher energy as the oxide buffer layer thickness is increased. The wavelength shifts (determined from a Gaussian fit to the PL spectra; see Section 4.1 for details) as a function of oxide thickness are shown in Figure 4.12. Because the O1-series and the O2-series were produced at separate times, the peak wavelength values cannot be compared between the two series, but the values can be compared between specimens in the same series. At a buffer thickness between 10 and 15 nm, the PL intensity and blueshift is saturated. The fact that there is a clear trend with increasing buffer thickness shows that the nanocrystal layers "sense" the presence of the adjacent

layers through at least 6 nm of oxide and maybe up to as much as 10 nm. Given these migration distances, we can assume that the nc-Si layers in the S-series specimens, which are separated by 20 nm of oxide, are well-isolated.

If it is accepted that the nanocrystal layers can interact through several nanometers of buffer oxide (there does not seem to be any other obvious explanation for the data), then one must have some mechanism by which such an effect can occur. There are several possible mechanisms for carrier migration between semiconductor nanoparticles that have been proposed and explored in the literature, although the great bulk of that work is for direct gap II-VI nanoparticles or porous silicon. In the following section, possible mechanisms are explored and future research plans are outlined to further elucidate the interaction mechanisms.

## 4.6 Interactive Nanocluster Model

The evidence presented in this chapter indicates that carrier migration occurs in the nc-Si specimens studied in this thesis. There are many experimental lines of evidence in favor of this process. Carriers transferring from one nanoparticle to another must result in excitation of sites with equal or lower energy, as indicated by the redshifted PL as the **active** buffer layers are made thinner. Similarly, the fairly dramatic enhancement of the luminescence intensity is due to more restricted carrier migration in thinner nanocrystal layers. The migration is also strongly evidenced in the E-series samples, in which relatively thick layers (nominally 20 nm) of nanoparticles are entirely quenched by adjacent $Er_2O_3$ layers. The clearly stretched exponential form of the S-series PL lifetime spectra suggests that migration occurs even in single planes of silicon nanoparticles (see specimen

S5). The O-series samples show that the nanocrystal layers can interact through as much as 6 nm and maybe up to 10 nm of intervening oxide.

To explain these results, this thesis proposes an "interactive nanocluster" model in which charge carriers can migrate between closely-spaced particles and can travel distances potentially as large as 10 nm. This migration distance is not unreasonable given estimates of ~9 nm for InP (Micic *et al.* 1998) and ~5 nm for CdSe (Kagan *et al.* 1996) quantum dots. In effect, the specimens investigated here may be a type of Coulomb glass (a spatially random array of localized charges in which long-range interaction between the charges is prominent; *e.g.*, Lee and Stutzmann 2001). The transfer mechanism between nanoparticles in these specimens cannot be unambiguously identified by the present experiments, but one can at least speculate on the possibilities. The interaction should depend on one or more of the following parameters: the nanocrystal size and separation, the confinement energy for electrons and holes, the energy levels associated with radiative centers and non-radiative traps at the nanocrystal-matrix interface, and the work function and dielectric constant of the matrix.

Several interaction mechanisms have been proposed in the literature. For example, Micic *et al.* (2001) observed the formation of lower-energy absorption features caused by extended states and mini-bands between nanocrystals separated by distances less than 1 nm. Another possibility is exciton tunnelling via resonant dipole-dipole interactions, which has been observed in quantum dot solids over distances of at least a nanometer (Bryant 2002) or more (Kagan *et al.* 1996). Individual charge carriers may also directly tunnel through the thin oxide barrier that separates nanoparticles. Vial *et al.* (1992) con-

sidered the tunneling of electrons in porous silicon, as holes were more likely to be confined by the high oxide barriers.

To attempt to model the PL wavelength shift, the electron-tunneling model of Vial *et al.* (1992) was used to determine the average transparency in each specimen of the X- and S-series. Firstly, a simplified view of the specimens was required, and a cubic lattice of 3-nm-diameter Si nanoparticles in a matrix of $SiO_2$ was chosen. The interparticle spacing was determined to be 3.3 nm by employing the constraint that the overall composition of the layer must be $SiO_{1.2}$ and this value is not inconsistent with the TEM images.

For a single layer of nanoparticles, there are four nearest-neighbours (the (100) direction) at a distance of 3.3 nm, four second-nearest-neighbours (110) at a distance of 5.9 nm, and zero third-nearest-neighbours (111) at a distance of 10.9 nm. The average number of nearest-neighbours per nanocrystal increases as a function of the layer thickness. Each type of neighbour will have an associated probability of carrier migration, and the transparency is proportional to this probability. For spherical particles, the transparency to tunneling, $T$, can be written as (Vial *et al.* 1992):

$$T = e^{\frac{-4\pi a\sqrt{m\left(V_0 + \frac{E_g}{3} - \frac{(E_g + 3\cdot E_e)}{3}\right)}}{h}} \qquad (4.1)$$

where $a$ is the barrier thickness (3.3 nm), $m$ is the effective mass of the electron inside the barrier, $V_0$ is the barrier height, $E_g$ is the bandgap width, $E_e$ is the electron confinement energy, and $h$ is Planck's constant. For a 3-nm-diameter particle, the optical gap is on the order of 2 eV (Delerue *et al.* 1999). It is difficult to estimate the barrier height exactly, especially since we don't know the exact composition of the barrier (based on the phase

diagram for the Si-O system, it is probably $SiO_2$, but it is not possible using EDS to get an independent measurement). Previous authors have suggested a reasonable barrier height of 3 eV for $SiO_2$ (Vial *et al.* 1992), and the same value will be used here. The electron confinement energy is estimated at 1.5 eV (Wolkin *et al.* 1999).

Since transparency is an exponential function of distance, using the above values we can see that the transparency decreases by approximately 4 to 5 orders of magnitude on going from the nearest-neighbours to the next-nearest-neighbours. Thus, for reasonable estimates of the energy levels, only the particles nearest each other are likely to interact through carrier tunneling.

Figure 4.13 shows the calculated transparency for layer thicknesses corresponding to specimens S1-S5 and X1-X4, plotted against the measured spectral blueshift. The X- and S-series data are fit to lines, each with strong positive correlation ($r^2$ is above 0.95 for both data sets). We see that as particles become, on average, more isolated in thinner layers, the probability of carrier migration decreases and the spectrum blueshifts. The strong correlation within two separate data sets suggests that the concept of quantum mechanical tunneling of electrons among neighbouring nanoparticles can potentially explain the layer thickness dependence of the photoluminescence. Differences between

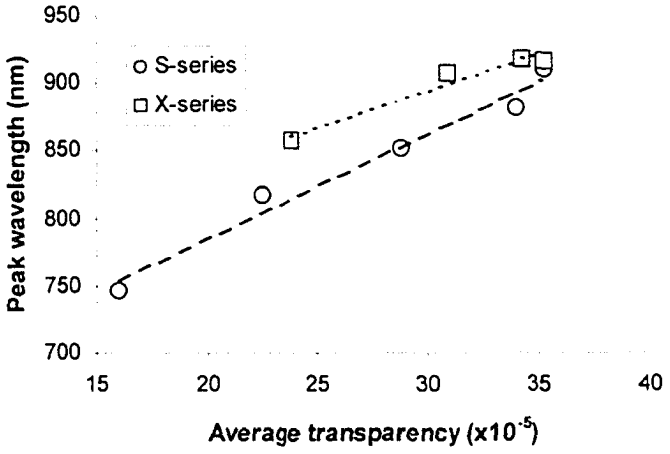


**Figure 4.13:** Peak wavelength varying according to average transparency, fitted to straight lines with confidence of 0.95.

the two data sets are probably due to particle size and spacing not being exactly the same between the X- and S-series.

Indeed, electron migration has been proposed by several researchers, in addition to Vial and colleagues, for various nanocrystalline semiconductors. Micic *et al.* (2001) found that a redshift in the absorption spectra of InP quantum dots occurred when the dots were more densely packed. They explained the results in terms of electron delocalization in the disordered, close-packed solids. Electronic energy transfer from small to large CdSe quantum dots was observed by Kagan *et al.* (1996). Therefore, it seems reasonable that electrons are the mobile charge carriers in our nc-Si specimens as well, as suggested by Vial et al. (1992) for porous silicon.

# Chapter 5: Wavelength Control

By varying the spacing and thickness of the nanocrystal layers, in this work I have obtained good control over the emission peak wavelength, with over 160 nm of spectral tunability for otherwise identical nanocrystals. To my knowledge, this if the first time that such wavelength tunability has been achieved through the exploitation of nanoparticle interactions alone (*i.e.*, without changing the nanoparticle size). Control of emission wavelength is an important feature for potential applications of silicon nanocrystals in photonic devices, such as light emitting diodes, optical amplifiers, optical displays, and possibly tunable quantum dot lasers. For most of these devices, not only does the peak wavelength have to be controllable, but additionally some control over the shape of the spectrum and additional tunability into the visible region would be important. In this final section of the thesis, I will describe some of my initial results towards these objectives. This work was done in close collaboration with other group members, including Aaron Hryciw and Josh LaForge.

The emission peaks of the nc-Si/$SiO_2$ superlattices are rather broad (~200 nm at the full-width-half-maximum), and only emission in the red to infrared has been achieved with nc-Si specimens annealed at 1000°C (see Figure 5.1). However, the emission of silicon nanocrystals can be both nar-

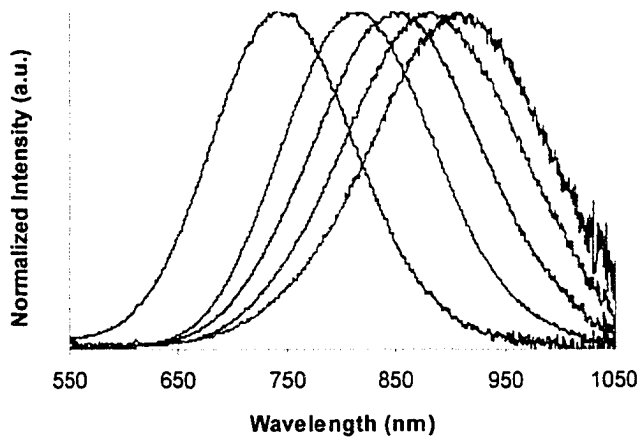


**Figure 5.1:** Normalized PL spectra of nc-Si/$SiO_2$ superlattices (S-series). The nanoparticle size distribution is the same in all specimens.

rowed and intensified by placing them within a distributed Bragg reflector. A distributed Bragg reflector is a multilayer structure used to obtain a high degree of reflection. When two such multilayer stacks, ideally with good refractive index contrast, are sandwiched around an emitting layer of appropriate thickness, a planar microcavity is formed.

A nc-Si resonant cavity from a distributed Bragg reflector was successfully made by Iacona *et al.* (2001a), who used alternating layers of silicon and silicon dioxide with thickness $\lambda/(4n)$ as the top and bottom mirrors. However, we found fabrication of the dielectric stacks to be very difficult, as the required precise control of the layer thicknesses could not be easily obtained in the multi-user experimental setup. Instead, we decided to simplify the system by using metal mirrors and a lower temperature thermal processing.

The initial investigations into optimization of synthesis procedures were carried out primarily by Josh LaForge and Aaron Hryciw of the University of Alberta. Initially, we intended to place a layer of nc-Si between the metal mirrors, but the high annealing temperature required to form nanocrystals became a problem: no metals with suitable reflective properties could withstand heat treatments at 1000°C. Therefore, we annealed all specimens at lower temperatures (500°C for this work). Other than that, the synthesis process I used was the same as for the nanocrystal specimens discussed in Chapters 2-4.

A suitable metal should be highly reflective at the emission wavelengths, but fairly transparent to the pump laser. Silver was chosen for the mirrors because it is highly reflective throughout the visible range and it has a good transmittance at the wavelength used for excitation (325 nm). As the reflectivity of silver is so high through most of the visible range (~98-99%), only single silver mirrors are required to sandwich the resonant cavity, unlike with dielectric mirrors which have such a low reflectivity that numerous layers are

required to provide adequate reflectance (although with enough layers, the reflectance of dielectric mirrors can be higher than for metals and there is ideally no absorption loss).

Metal mirrors, unlike dielectric mirrors, will induce a phase change in light reflected from their surfaces. The standard phase factor upon reflection from parallel mirrors is given by

$$\phi = kz = 2kd\cos\theta \tag{5.1}$$

where $k$ is the wavenumber ($k = (2\pi)/\lambda$ in free space or $(2\pi n)/\lambda$ in a medium of refractive index $n$), $d$ is the thickness of the active layer, $\theta$ is the angle of incidence, and $z$ is the path length for the reflected wave to return to the original location and direction ($z = 2d\cos\theta$). This expression assumes that there is no additional phase shift upon reflection at the mirrors. In order to obtain constructive interference, the total phase shift must be an integer ($m$) multiple of $2\pi$, or

$$2kd\cos\theta = 2\pi m \tag{5.2}$$

However, metal mirrors do have phase shifts upon reflection. According to Djurisic and Rakic (2002), the constructive interference condition can then be given by

$$2kd\cos\theta - \phi_1 - \phi_2 = 2\pi m \tag{5.3}$$

where $\phi_1$ and $\phi_2$ are the phase changes from the two metal surfaces. This version will lead to positive mode numbers; however many publications instead choose to write the same formula as

$$-2kd\cos\theta + \phi_1 + \phi_2 = 2\pi m \tag{5.4}$$

which leads to negative mode numbers (e.g., see Jung *et al.* 2002). Rearranging terms and solving for $\lambda$ (in the positive case) gives:

$$\lambda = \frac{4\pi nd\cos\theta}{2\pi m + \phi_1 + \phi_2} \qquad (5.5)$$

This expression reduces to

$$m\lambda = 2nd \qquad (5.6)$$

for the zero phase change condition at normal incidence. For metals, however, there are significant phase changes that are not zero or integer multiples of $\pi$, and the mode numbers can therefore start at zero (*i.e.*, $m = 0$ provides a valid solution for the resonance condition in equation 5.5, due to the phase changes at the reflecting surfaces).

The optical phase change depends upon the complex refractive index of the metal mirrors and is therefore wavelength dependent. For this project, characteristic optical matrix calculations were set up by Josh LaForge, Aaron Hryciw, and Al Meldrum using various software routines. These require as input only the wavelength-dependent refractive indices and film thicknesses, and the resonant modes are calculated directly. This enabled me to easily obtain the active layer thickness for a given resonance wavelength. We used the tabulated optical constants for silver and SiO in order to estimate the film thicknesses needed to produce a reasonable range of resonant wavelengths.

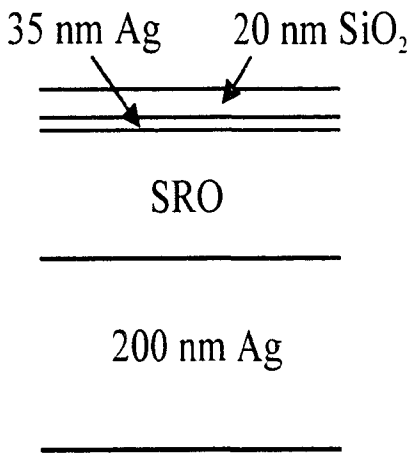


**Figure 5.2:** Schematic of an optical cavity. The SRO layer thickness is chosen to give the desired resonant emission wavelength.

Four optical cavity specimens (C1-C4) were prepared. The Bragg reflectors consisted of a nominally 200-nm-thick silver mirror below the SRO layer, and a 35-nm-thick

silver mirror plus a 20-nm-thick protective silicon dioxide layer on top (see Figure 5.2). The bottom mirror was made thick to maximize its reflectivity, while the top mirror was made thin so that could function as an output coupler. The layers were deposited using the electron beam evaporation method described in Chapter 2, although the silver layers were not deposited in a partial pressure of oxygen. The bottom silver layer and the SRO layer were annealed at 500° C and the top mirror and protective oxide coating were deposited after annealing. The SRO layer thicknesses were chosen to provide certain emission wavelengths. For each cavity (specimens C1-C4) the layer thicknesses and their corresponding emission wavelengths (as shown in Figure 5.4) are listed in Table 5.1.

**Table 5.1:** Active layer thicknesses for specimens C1-C4, and the emission wavelengths (as shown in Figure 5.4) of the cavities. Specimen C1 emits at a longer wavelength than the thicker specimens because the emission is first-order ($m = 0$), not second-order ($m = 1$) like C2-C4.

| Specimen | Layer thickness (nm) | Emission wavelength (nm) |
|---|---|---|
| C1 | 197 | ~812 |
| C2 | 254 | ~525 |
| C3 | 311 | ~615 |
| C4 | 367 | ~685 |

At these low processing temperatures, initial TEM results suggest the presence of amorphous silicon clusters. We found that the samples emit a broad luminescence that is shifted toward the visible, as compared with the nanocrystals produced at higher temperatures (Figure 5.3). This broad luminescence is useful, as a cavity can be tuned to any wavelength within the intrinsic luminescence spectrum.

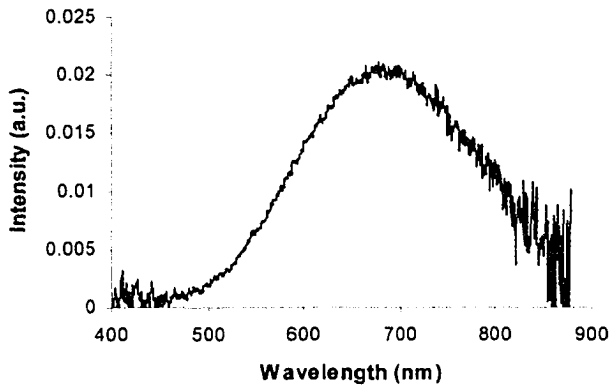


**Figure 5.3:** Broad PL spectrum from a $SiO_x$ specimen annealed at 500°C.

The photoluminescence of four optical cavities with SRO as the active material are shown in Figure 5.4. The PL spectra were collected normal to the specimen surface and are much narrower (FWHM ~ 13 nm) than the superlattice PL. The wavelength was tuned over a range of 300 nm simply by changing the SRO layer thickness. This initial attempt at extended wavelength tunability was a direct consequence of the work in the previous chapters, which showed that the intrinsic PL peak could not be shifted into the visible spectrum in any of my samples. Aaron Hryciw has now done the bulk of the work on the microcavity devices and we have a paper, lead-authored by Aaron, now in press in the journal *Advanced Materials*.

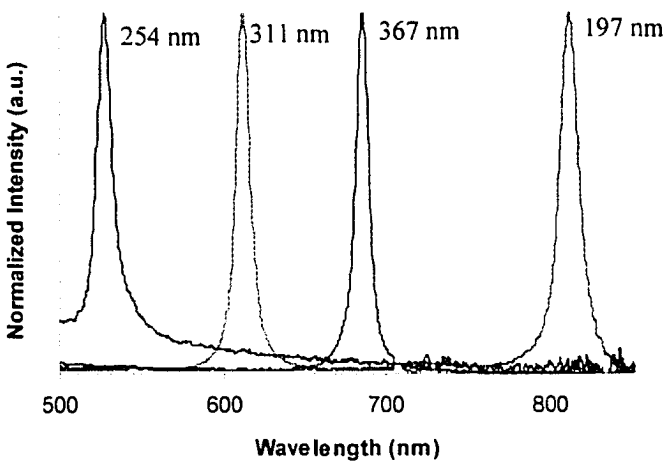


**Figure 5.4:** Normalized PL spectra of four Ag/SRO optical cavities (C1-C4), with the corresponding SRO layer thickness labeled beside each curve.

# Chapter 6: Conclusions

We have seen that nanocrystalline silicon specimens with good luminescence can be prepared by electron-beam evaporation of SiO in a partial pressure of $O_2$, followed by thermal processing. These nanocrystals emit visible-to-infrared light whose peak wavelength can be tuned by over 160 nm without changing the size of the nanocrystals.

The luminescence is not consistent with direct exciton recombination across the nc-Si bandgap, as no significant emission peak shift is observed with size selection by pump wavelength. Instead, there is a major shift in the photoluminescence peak energy due to the addition of buffer layers that separate the active (nanocrystalline) material. These results do not agree with a pure quantum confinement model for the emission. The results contradict the interpretations made in a considerable amount of previous literature (for examples, see Brongersma *et al.* 1999; Min *et al.* 1996) in which redshifts in specimens with larger particles were attributed to size effects. In those publications, however, size effects were not separated from *proximity* effects - specimens with larger particles were made by increasing the density of active material, which in turn should change the interparticle spacing. This is the first investigation in silicon nanocrystal superlattices in which the nanocrystal size was kept the same, thus systematically isolating size effects from proximity effects.

The photoluminescence results show that the spacing of the active layers and the buffer layers has significant influence on the specimen optical properties. In the X- and S-series, carrier migration occurs within the nc-Si layers, as evidenced by the stretched exponential form of the luminescence lifetime results. Reducing the nanocrystal layer thickness in turn reduces carrier migration, which causes a PL spectral blueshift with

decreasing nc-Si layer thickness. This spectral blueshift cannot be the result of a change in nanoparticle size, as the average particle size was essentially the same within all specimens of the same series due to preparing them under identical conditions. In the O-series, the nanocrystal layers are well isolated when the $SiO_2$ buffer layers are 10 nm thick or more. The E-series provides convincing evidence in favor of carrier migration through the nanocrystal layers. In that example, 20-nm-thick films of nanocrystals could be totally quenched by adjacent $Er_2O_3$ layers, suggesting a kind of particle-to-particle "hopping" mechanism that can transfer charge carriers over significant distances.

As the results from the X- and S-series specimens indicate that carrier migration occurs within the layer of Si nanoparticles, this work proposed an "interactive nanocluster model". This is not the first hint of such a mechanism in silicon nanocrystal composites, but I believe that it is the most systematic study to date on the interactive nanocluster model (a term coined in this thesis). In this model, charge carriers can migrate between nearby nanocrystals, and this can qualitatively account for the observed spectral shifts and changes in emission intensity in the different specimens. Although we have no *direct* evidence to indicate what types of carriers are migrating, results in the literature are more consistent with electron migration as opposed to holes or bound excitons. The excellent correlation between the present data and the model of Vial *et al.* for quantum mechanical tunneling of electrons also lends support to this hypothesis.

In terms of wavelength tunability, the superlattices studied in this thesis have covered what appears to be the full wavelength range possible for these specimens. The PL spectra of the single layer nc-Si films indicate that there will not be much, if any, interaction-induced spectral shift for layers more than 200 nm thick since such thick films are

essentially akin to a "bulk" nanocomposite material. Specimens cannot be made thinner than a single layer of nanoparticles, and so no further wavelength shift can be achieved beyond specimen S5 either. One could envision trying to isolate the nanoparticles in all three dimensions; however, this would be very challenging experimentally and would almost certainly require some serious lithography-based processes to be developed (or, possibly, a chemical approach). Nevertheless, as discussed in Chapter 5, a much wider range of emission wavelengths can be achieved using optical cavities with SRO as the active layer. These emission peaks are also quite narrow, which is also a desirable feature for potential technological applications. The cavities, with their metal mirrors, are also much simpler to prepare than the dielectric stacks. Work is already underway amongst other members of this research group to study and refine the emission from these optical cavities, including synthesizing specimens in which wavelength tunability is available within a single optical cavity.

Potential extensions of this study could involve a more accurate measurement of the nanocrystal photoluminescence lifetimes, and possibly measuring the wavelength dependence of the lifetime. Measuring the lifetime of the erbium infrared photoluminescence would be helpful for developing and solving rate equations - for example, one could envision calculating a "lifetime" for the particle-to-particle transfer process. This would be important since both the basic physics and many of the practical applications of silicon nanocrystal composites will depend on migration effects. Certainly the door seems open for future quantitative investigations into the optical properties of silicon nanocrystal superlattices.

A study of nc-Si specimens using THz spectroscopy is currently being done in Frank Hegmann's laboratory at the University of Alberta. Those specimens were prepared on the basis of the procedures developed in this thesis. Terahertz spectroscopy is an established method for measuring carrier mobilities on a time scale as short as picoseconds, and the results may shed further light on the effects and mechanisms of carrier transfer (although the effects of surface trapping may be expected to be important at such short time scales).

As a final word, it is probably important to make a comment on the complex physics at work in silicon nanocrystals. For almost 15 years people have been arguing (sometimes almost fighting) over the emission mechanism for silicon nanocrystals embedded in a matrix of $SiO_2$. What has been learned unequivocally is that the situation is highly complicated and many factors must be examined and isolated from one another. It is almost certain, for example, that numerous previous authors could have confused particle proximity effects for particle size effects, as discussed in this thesis. This really highlights the need for extremely careful and systematic approaches, especially with regards to the specimen preparation. Even in this thesis, we found that the slightest variations in the experimental setup in the electron beam evaporator could lead to significant PL shifts. Any future work really needs to take such factors into consideration and put extreme care into the specimen preparation and interpretation of the results - something which, from a careful survey of the literature, has not always been done.

# References

Allan, G., Delerue, C., and Lannoo, M. (1996) Nature of luminescent surface states of semiconductor nanocrystallites: Physical Review Letters, 76, 2961-2964.

Brongersma, M.L., Polman, A., Min, K.S., and Atwater, H.A. (1999) Depth distribution of luminescent Si nanocrystals in Si implanted $SiO_2$ films on Si: Journal of Applied Physics, 86, 759-763.

Brus, L.E., Szajowski, P.F., Wilson, W.C, Harris, J.D., Schuppler, S., and Citrin, P.H. (1995) Electronic spectroscopy and photophysics of Si nanocrystals - Relationship to bulk C-Si and porous Si: Journal of American Chemical Society, 117, 2915-2922.

Bryant, G.W. (2002) Physica B, 314, 15.

Chen, R. (2003) Apparent stretched-exponential luminescence decay in crystalline solids: Journal of Luminescence, 102, 510-518.

Cheylan, S. and Elliman, R.G. (1999) The effect of ion dose and annealing ambient on room temperature photoluminescence from Si nanocrystals in $SiO_2$: Nuclear Instruments And Methods In Physics Research Section B - Beam Interactions With Materials And Atoms, 148, 986-990.

Coffa, S., Polman, A., and Schwartz, R.N. (Eds.) (1996) Materials Research Society Symposium Proceedings, 422.

Delerue, C., Allan, G., and Lannoo, M. (1993) Theoretical aspects of the luminescence of porous silicon: Physical Review B, 48, 11024-11036.

Delerue, C. Allan, G., and Lannoo, M. (1999) Optical band gap of Si nanoclusters: Journal of Luminescence, 80, 65-73.

Delerue, C., Allan, G., and Lannoo, M. (2001) Electron-phonon coupling and optical transitions for indirect-gap semiconductor nanocrystals: Physical Review B, 64, art. no. 193402.

Delerue, C., Allan, G., and Lannoo, M. (2003) Theory of silicon nanocrystals. In Towards the First Silicon Laser, L. Pavesi, S. Gaponenko, and L. Dal Negro (Eds.), NATO Science Series II. Mathematics, Physics, and Chemistry - Vol. 98, Kluwer Academic Publishers, pp. 243-260

Djurisic, A.B. and Rakic, A.D. (2002) Organic microcavity light-emitting diodes with metal mirrors: dependence of the emission wavelength on the viewing angle: Applied Optics, 41, 7650-7656.

Elliman, R.G., Lederer, M.J., Smith, N., and Luther-Davies, B. (2003) The fabrication and properties of silicon-nanocrystal-based devices and structures produced by ion implantation - The search for gain: Nuclear Instruments and Methods in Physics Research B - Beam Interactions With Materials and Atoms, 206, 427-431.

Ennen, H., Schneider, J., Pomrenke, G., and Axmann, A. (1983) 1.54-mu-m Luminescence of Erbium-implanted III-V Semiconductors and Silicon: Applied Physics Letters, 43, 943-945.

Franzo, G., Vinciguerra, V., and Priolo, F. (1999) The excitation mechanism of rare-earth ions in silicon nanocrystals: Applied Physics A - Materials Science and Processing, 69, 3-12.

Fujii, M., Yoshida, M., Hayashi, S., and Yamamoto, K. (1998) Photoluminescence from $SiO_2$ films containing Si nanocrystals and Er: Effects of nanocrystalline size on the photoluminescence efficiency of $Er^{3+}$: Journal of Applied Physics, 84, 4525-4531.

Garrido, B., Lopez, M., Gonzalez, O., Perez-Rodriguez, A., Morante, J.R., and Bonafos, C. (2000) Correlation between structural and optical properties of Si nanocrystals embedded in $SiO_2$: The mechanism of visible light emission: Applied Physics Letters, 77, 3143-3145.

Hill, N.A. and Whaley, K.B. (1995) Size dependence of excitons in silicon nanocrystals: Physical Review Letters, 75, 1130-1133.

Hryciw, A., White, C.W., Chow, K.H., and Meldrum, A. (2003) Materials Research Society Symposium Proceedings, 777, 3.

Hryciw, A., Buchanan, K.S., Meldrum, A., and White, C.W. (2004) Effects of particle size and excitation spectrum on the photoluminescence of silicon nanocrystals formed by ion implantation: Nuclear Instruments and Methods in Physics Research B: Beam Interactions with Materials and Atoms, 222(3-4), 469-476.

Huy, B., Binh, P.H., Diep, B.Q., and Luong, P.V. (2003) Effect of ageing on the luminescence intensity and lifetime of porous silicon: roles of recombination centers: Physica E - Low Dimensional Systems and Nanostructures, 17 (1-4), 134-136.

Hybertsen, M.S. (1994) Absorption and emission of light in nanoscale silicon structures: Physical Review Letters, 72, 1514-1517.

Iacona, F, Franzo, G., Moreira, E.C., Pacifici, D., Irrera, A., and Priolo, F. (2001a) Luminescence properties of Si nanocrystals embedded in optical microcavities: Materials Science and Engineering C - Biomimetic and Supramolecular Systems, 19 (1-2), 377-381.

Iacona, F., Franzo, G., Vinciguerra, V., Irrera, A., and Priolo, F. (2001b) Influence of the spatial arrangement on the quantum confinement properties of Si nanocrystals: Optical Materials, 17, 51-55.

Iwayama, T.S., Kurumado, N., Hole, D.E., and Townsend, P.D. (1998) Optical properties of silicon nanoclusters fabricated by ion implantation: Journal of Applied Physics, 83, 6018-6022.

Iwayama, T.S., Hole, D.E., and Boyd, I.W. (1999) Mechanism of photoluminescence of Si nanocrystals in $SiO_2$ fabricated by ion implantation: the role of interactions of nanocrystals and oxygen: Journal of Physics: Condensed Matter, 11, 6595-6604.

Iwayama, T.S., Hama, T., Hole, D.E., and Boyd, I.W. (2001) Characteristic photoluminescence properties of Si nanocrystals in $SiO_2$ fabricated by ion implantation and annealing: Solid-State Electronics, 45, 1487-1494.

Kagan, C.R., Murray, C.B., and Bawendi, M.G. (1996) Long-range resonance transfer of electronic excitations in close-packed CdSe quantum-dot solids: Physical Review B, 54, 8633-8643.

Kagan, C.R., Bawendi, C.B., Nirmal, M., and Bawendi, M.G. (1996) Electronic Energy Transfer in CdSe Quantum Dot Solids: Physical Review Letters, 76, 1517-1520.

Kahler, U., and Hofmeister, H. (2001) Visible light emission from Si nanocrystalline composites via reactive evaporation of SiO: Optical Materials, 17, 83-86.

Kenyon, A.J., Trwoga, P.F., Pitl, C.W., and Rehm, G. (1998) Luminescence efficiency measurements of silicon nanoclusters: Applied Physics Letters, 73, 523-525.

Kenyon, A.J., Chyssou, C.E., Pitt, C.W., Iwayama, T.S., Hole, D.E., Sharma, N., and Humphreys, C.J. (2002) Luminescence from erbium-doped silicon nanocrystals in silica: Excitation mechanisms: Journal of Applied Physics, 91, 367-374.

Klimov, V.I., Schwarz, Ch.J., McBranch, D.W., and White, C.W. (1998) Initial carrier relaxation dynamics in ion-implanted Si nanocrystals: Femtosecond transient absorption study: Applied Physics Letters, 73, 2603-2605.

Klimov, V.I., Mikhailovsky, A.A., Xu, S., Malko, A., Hollingsworth, J.A., Leatherdale, C.A., Eisler, H.-J., and Bawendi, M.G. (2000) Optical gain and stimulated emission in nanocrystal quantum dots: Science, 290, 314-317.

Kovalev, D., Heckler, H., Ben-Charin, M., Polisski, G., Schwartzkopff, M., and Koch, F. (1998) Breakdown of the k-conservation rule in Si-nanocrystals: Physical Review Letters, 81, 2803-2806.

Jung, B.Y., Kim, N.Y., Lee, C., Hwangbo, C.K., and Seoul, C. (2002) Control of resonant wavelength from organic light-emitting materials by use of a Fabry-Perot microcavity structure: Applied Optics, 41, 3312-3318.

Lee, M. and Stutzmann, M.L. (2001) Microwave ac Conductivity Spectrum of a Coulomb Glass: Physical Review Letters, 87, art. no. 056402.

Linnros, J., Lalic, N., Galeckas, A., and Grivickas, V. (1999) Analysis of the stretched exponential photoluminescence decay from nanometer-sized silicon crystals in $SiO_2$: Journal of Applied Physics, 86, 6128-6134.

Lockwood, D.J., and Pavesi, L. (2004) Silicon fundamentals for photonics applications: Topics in Applied Physics, 94, 1-50.

Lopez, M., Garrido, B., Bonafos, C., Perez-Rodriguez, A., Morante, J.R., and Claverie, A. (2001) Model for efficient visible emission from Si nanocrystals ion beam synthesized in $SiO_2$: Nuclear Instruments and Methods in Physics Research Section B: Beam Interaction, 178, 89-92.

Lopez, M, Garrido, B., Garcia, C., Pellegrino, P., Perez-Rodriguez, A., Morante, J.R., Bonafos, C., Carrada, M., and Claverie, A. (2002) Elucidation of the surface passivation role on the photoluminescence emission yield of silicon nanocrystals embedded in $SiO_2$: Applied Physics Letters, 80, 1637-1639.

Macic, O.I., Jones, K.M., Cahill, A., Nozik, A.J. (1998) Optical, Electronic, and Structural Properties of Uncoupled and Close-Packed Arrays of InP Quantum Dots: Journal of Physical Chemistry B, 102, 9791-9766.

Meldrum, A. (2004) Silicon Nanocrystals: submitted.

Micic, O.I., Ahrenkiel, S.P., and Nozik, A.J. (2001) Applied Physics Letters, 78, 4022-4024.

Mihalescu, I., Vial, J.C., and Romestain, R. (1996) Carrier localization in porous silicon investigated by time-resolved luminescence analysis: Journal of Applied Physics, 80, 2404-2411.

Min, K.S., Shchlegov, K.V., Yang, C.M., Atwater, H.A., Bongersma, M.L., and Polman, A. (1996) Defect-related versus excitonic visible light emission from ion beam synthesized Si nanocrystals: Applied Physics Letters, 69, 2033-2035.

Neufeld, E., Wang, S., Apetz, R., Buchal, Ch., Carius, R., White, C.W., and Thomas, D.K. (1997) Effect of annealing and $H_2$ passivation on the photoluminescence of Si nanocrystals in $SiO_2$: Thin Solid Films, 294, 238-241.

Okada, T. and Ohta, E. (2002) Visible Photoluminescence from Evaporated $SiO_x$ Thin Films: Japanese Journal of Applied Physics, 41, 6413-6416.

Pavesi, L. (1996) Influence of dispersive exciton motion on the recombination dynamics in porous silicon: Journal of Applied Physics, 80, 216-225.

Pavesi, L. and Cheschini, M (1993) Stretched-exponential decay of the luminescence in porous silicon: Physical Review B, 48, 17625-17628.

Pavesi, L., Dal Negro, L., Mazzoleni, C., Franzo, G., and Priolo, F (2000) Optical gain in silicon nanocrystals: Nature, 408, 440-444.

Polman, A. (1997) Erbium implanted thin film photonic materials: Journal of Applied Physics, 82, 1-39.

Priolo, F., Franzo, G., Iacona, F., Pacifici, D., and Vinciguerra, V. (2001a) Excitation and non-radiative de-excitation processes in Er-doped Si nanocrystals: Materials Science and Engineering B - Solid State Materials For Advanced Technology, 81, 9-15.

Priolo, F., Franzo, G., Pacifici, D., Vinciguerra, V., Iacona, F., and Irrera, A. (2001b) Role of the energy transfer in the optical properties of undoped and Er-doped interacting Si nanocrystals: Journal of Applied Physics, 89, 264-272.

Sharma, N., Kenst, V.J., Iwayama, T.S., Boyd, I., and Humphreys, C.J. (1999) Electron Microscopy and Analysis 1999, Institute of Physics Conference Series, 161, 589.

Soni, R.K., Fonseca, L.F., Resto, O., Buzaianu, M., and Weisz, S.Z. (1999) Size-dependent optical properties of silicon nanocrystals: Journal of Luminescence, 83, 187-191.

Tsybeskov, L., Grom, G.F., Fauchet, P.M., McCaffrey, J.P., Bariobeau, J.-M., Sproule, G.I., Lockwood, D.J. (1999) Applied Physics Letters, 75, 2265.

Vala, A.S., Godfrey, M.J., and Dawson, P. (2001) Effects of Indium Segregation and Well-Width Fluctuations on Optical Properties of InGaN/GaN Quantum Wells: Physica status solidi (b) - Basic research, 228, 453-456.

Valenta, J., Pelant, I., and Linnros, J. (2002) Waveguiding effects in the measurement of optical gain in a layer of Si nanocrystals: Applied Physics Letters, 81, 1396-1398.

Vasiliev, I., Chelikowski, J.R., and Martin, R.M. (2002) Surface oxidation effects on the optical properties of silicon nanocrystals: Physical Review B, 65, art. no. 121302.

Vial, J.C., Bsiesy, A., Gaspard, F., Herino, R., Ligeon, M., Muller, F., Romestain, R., and Macfarlane, R.M. (1992) Mechanisms of visible-light emission from electro-oxidized porous silicon: Physical Review B, 45, 14171-14176.

Vinciguerra, V., Franzo, G., Priolo, F., Iacona, F., and Spinella, C. (2000) Quantum confinement and recombination dynamics in silicon nanocrystals embedded in $Si/SiO_2$ superlattices: Journal of Applied Physics, 87, 8165-8173.

White, C.W., Budai, J.D., Withrow, S.P., Zhu, J.G., Sonder, E., Zuhr, R.A., Meldrum, A., Hembree, D.M., Henderson, D.O., and Prawer, S. (1998) Encapsulated semiconductor nanocrystals formed in insulators by ion beam synthesis: Nuclear Instruments and Methods in Physics Research Section B: Beam Interaction, 141, 228-240.

Wilcoxon, J.P., Samara, G.A., and Provencio, P.N. (1999) Optical and electronic properties of silicon nanoclusters synthesized in inverse micelles: Physical Review B, 60, 2704-2714.

Williams, D.B. and Carter, C. (1996) Transmission Electron Microscopy: A textbook for Materials Science, Plenum, New York, pp.599-604.

Withrow, S.P., White, C.W., Meldrum, A., Budai, J.D., Hembree Jr., D.M. and Barbour, J.C. (1999) Effects of hydrogen in the annealing environment on photoluminescence from Si nanoparticles in $SiO_2$: Journal of Applied Physics, 86, 396-401.

Wolkin, M.V., Fauchet, P.M., Allan, G., and Delerue, C. (1999) Electronic states and luminescence in porous silicon quantum dots: The role of oxygen: Physical Review Letters, 82, 197-200.

Yanagiya, S. et al. (1994) Materials Research Society Symposium Proceedings 316, 487.

Yi, L.X., Heitmann, J., Scholz, R., and Zacharias, M. (2002) Si rings, Si clusters, and Si nanocrystals - different states of ultrathin $SiO_x$ layers: Applied Physics Letters, 81, 4248-4250.

Zacharias, M., Heitmann, J., Scholz, R., Kahler, U., Schmidt, M., and Blasing, J. (2002) Size-controlled highly luminescent silicon nanocrystals: A $SiO/SiO_2$ superlattice approach: Applied Physics Letters, 80, 661-663.

# Appendix: Fitted Photoluminescence Spectra Results

As discussed briefly in Section 4.1, in order to obtain the value of the peak wavelength for the photoluminescence spectra of the X-, S-, and O-series specimens, a least-squares algorithm developed in MatLab was used to fit a Gaussian functional form to each PL spectrum. The function fit to each spectrum was:

$$G = a_p \cdot e^{\frac{(\lambda - \lambda_p)^2}{\sigma^2}} \qquad \text{(A.1)}$$

where $a_p$ is the peak intensity of the spectrum, $\lambda$ is wavelength, with $\lambda_p$ being the peak wavelength, and $\sigma$ is the full-width-at-half-maximum (FWHM). Photoluminescence spectra were fit to the raw PL data from the X-, S-, and O-series specimens, and also to the six PL spectra of specimen S1 at different excitation wavelengths, and to the PL spectra of the S-series specimens excited at different powers. The integrated intensity (summing under the curve) was used instead of the Gaussian peak intensity $a_p$, and it is listed in the tables below. Table A.1 lists the fitted values for X-, S-, and O-series specimens; Table A.2 lists the values for the excitation-wavelength-dependent spectra; and Table A.3 lists peak wavelengths and integrated intensities for the power-dependent spectra.

**Table A.1:** Peak wavelength, integrated intensity, and full-width-at-half-maximum (FWHM) values from fits of a Gaussian form to PL spectra of specimens from the X-, S-, and O-series. The intensity was integrated between: 650 - 1050 nm for X-series, 550 - 1000 nm for S-series, 650 - 1000 nm for O1-series, and 700 - 1000 nm for O2-series.

| Specimen | Peak wavelength $\lambda_p$ (nm) ±1 nm | Integrated intensity (a.u.) | FWHM $\sigma$ (nm) ±2 nm |
|---|---|---|---|
| X1 | 916 | 713 | 73 |
| X2 | 918 | 403 | 74 |
| X3 | 908 | 444 | 74 |
| X4 | 858 | 304 | 78 |
| S1 | 911 | 177 | 83 |
| S2 | 883 | 382 | 81 |
| S3 | 852 | 558 | 78 |
| S4 | 817 | 858 | 70 |
| S5 | 747 | 185 | 68 |
| O1a | 882 | 363 | 83 |
| O1b | 855 | 570 | 82 |
| O1c | 850 | 547 | 81 |
| O1d | 847 | 568 | 83 |
| O2a | 887 | 403 | 78 |
| O2b | 887 | 391 | 78 |
| O2c | 885 | 487 | 76 |
| O2d | 881 | 553 | 76 |

**Table A.2:** Fitted values of peak wavelength, integrated intensity, and full-width-at-half-maximum for the excitation dependent photoluminescence spectra of specimen S1. The intensity was integrated between 650 - 1000 nm.

| Excitation wavelength (nm) | Peak wavelength $\lambda_p$ (nm) ±1 nm | Integrated intensity (a.u.) | FWHM $\sigma$ (nm) ±2 nm |
|---|---|---|---|
| 325 | 907 | 154 | 85 |
| 442 | 908 | 103 | 80 |
| 456 | 918 | 78 | 87 |
| 476 | 921 | 61 | 86 |
| 488 | 922 | 49 | 85 |
| 514 | 921 | 46 | 84 |

**Table A.3:** Peak wavelength, $\lambda_p$ (±1 nm), and integrated intensity, I (a.u.), values for the S-series specimens at excitation powers of 100 - 1000 mW. The intensity was integrated between 550 - 1050 nm.

| Power (mW) | S1 | | S2 | | S3 | | S4 | | S5 | |
|---|---|---|---|---|---|---|---|---|---|---|
| | $\lambda_p$ | I | $\lambda_p$ | I | $\lambda_p$ | I | $\lambda_p$ | I | $\lambda_p$ | I |
| 100 | 880 | 57 | 873 | 107 | 844 | 84 | 813 | 128 | 746 | 19 |
| 200 | 875 | 86 | 868 | 156 | 839 | 129 | 809 | 195 | 744 | 31 |
| 300 | 871 | 107 | 866 | 189 | 836 | 166 | 807 | 251 | 743 | 42 |
| 400 | 868 | 125 | 863 | 215 | 834 | 195 | 805 | 297 | 741 | 51 |
| 500 | 866 | 138 | 862 | 233 | 832 | 221 | 803 | 339 | 740 | 59 |
| 600 | 864 | 149 | 861 | 247 | 830 | 244 | 802 | 373 | 739 | 66 |
| 700 | 862 | 160 | 859 | 259 | 829 | 266 | 801 | 409 | 739 | 73 |
| 800 | 860 | 170 | 859 | 267 | 828 | 284 | 801 | 437 | 738 | 79 |
| 900 | 859 | 177 | 858 | 271 | 827 | 300 | 800 | 463 | 737 | 84 |
| 1000 | 858 | 182 | 859 | 274 | 827 | 314 | 800 | 486 | 737 | 89 |